

DRAFT

ROYAL HOLLOWAY UNIVERSITY OF LONDON

M.SC THESIS

STUDENT ID: 100920158

**Comparative Analysis of Simulations and
Experimental Outcomes: Slow Extraction Driven by
RF Transverse Excitation at the CERN Proton
Synchrotron**

Author:

Thomas BASS

Supervisor:

Professor Stephen GIBSON

July 5, 2023



Contents

1	Introduction	4
1.1	Motivation	6
1.1.1	Extraction Methods	6
1.1.2	Introduction to Slow Extraction	8
1.2	Modelling Slow Extraction	8
2	Accelerator Physics Theory	10
2.1	Transverse Beam Dynamics	10
2.1.1	Coordinate System	10
2.1.2	Special Relativity	11
2.1.3	Particle Variables	12
2.1.4	Design orbit and Dipoles	12
2.1.5	Focussing and Multipoles	14
2.1.6	Single-Particle Oscillatory Motion	15
2.1.7	Phase Space	17
2.1.8	Dispersion	18
2.1.9	Matrix Formalism	19
2.1.10	Normalised Phase Space	20
2.2	Longitudinal Dynamics	20
2.2.1	Magnetic Ramping	20
2.2.2	Dispersion	21
2.2.3	Longitudinal Phase Space	22
2.3	Slow Extraction	22
2.3.1	Sextupoles and $\frac{1}{3}$ -Integer Resonance	22
2.3.2	Slow Extraction Principles	25

DRAFT

2.3.3	Steinbach Diagram	26
2.3.4	Slow Extraction Methods	27
3	Implementation and Simulation	31
3.1	RFKO Slow Extraction at the CERN PS	31
3.1.1	Closed Orbit and Extraction Trajectory	31
3.1.2	Magnetic Cycle	32
3.1.3	Transverse Excitation	35
3.2	RFKO Slow Extraction in Simulation	36
3.2.1	Simulation Tools	36
3.2.2	Lattice Configuration	37
3.2.3	Distribution Generation	38
3.2.4	Simulation Process	39
4	Analysis	41
4.1	Computation Time	41
4.2	Frequency Response	41
4.3	Spill Duty Factor	42
5	Conclusion	45
6	Acknowledgements	46
A	Derivations	50
A.1	Relating longitudinal variables	50
B	Code Snippets	51
C	Data and Plots	53

DRAFT

ABSTRACT

Resonant slow extraction is a beam extraction method which provides a continuous spill over a longer duration than can be achieved with fast single-turn or non-resonant multi-turn extraction. By using transverse excitation to drive the circulating particles onto the resonance, long-duration spills can be produced, and delivered to facilities such as fixed-target experiments, or hadron therapy gantries.

In order to accurately and efficiently simulate the extraction process over a wide range of timescales, new modelling tools and computing platforms must be explored. By utilising optimised computational hardware—such as General Purpose Graphics Processing Units (GPGPUs), and next-generation simulation software (such as Xsuite), computation times for simulations can be reduced by several orders of magnitude.

This thesis presents recent developments of resonant slow extraction modelling and benchmarking with a comparison to measurements made at CERN’s Proton Synchrotron (PS), with a particular focus on understanding the dynamics of transverse RF excitation and effect on spill quality.

Keywords Beam Physics, Slow Extraction, Radio-Frequency Knock-Out, Simulation, Xsuite

Chapter 1

Introduction

The CERN Proton Synchrotron (PS), alongside providing intermediary acceleration for hadron and ion beams for the Super Proton Synchrotron (SPS) and eventually the Large Hadron Collider (LHC), provides beams for the many fixed target experiments located at the East Area (EA) experimental facility. This facility, as illustrated in Figure 1.1, consists of the proton (IRRAD) and mixed-field (CHARM) irradiation facilities, via a dedicated 24 GeV/c beamline, in addition to a multi-target beamline providing three secondary beams.

Ongoing experiments in these facilities such as the CHARM High-energy Ions for Micro Electronics Reliability Assurance (CHIMERA) [1] use high-Z ions (Pb) to simulate the harsh radiation environment of cosmic rays which satellites experience. Using low-intensity ($<10^6$ ions/spill), high-energy (>100 MeV/u) beams, customers such as the European Space Agency can assess the reliability of new materials in these environments. Figure 1.2 illustrates the two injection chains of the PS, either with Lead ions sourced from the Linear Accelerator 3 (Linac3) and Low Energy Ion Ring (LEIR) chain, or protons from the Linac4 and the Proton Synchrotron Booster (PSB).

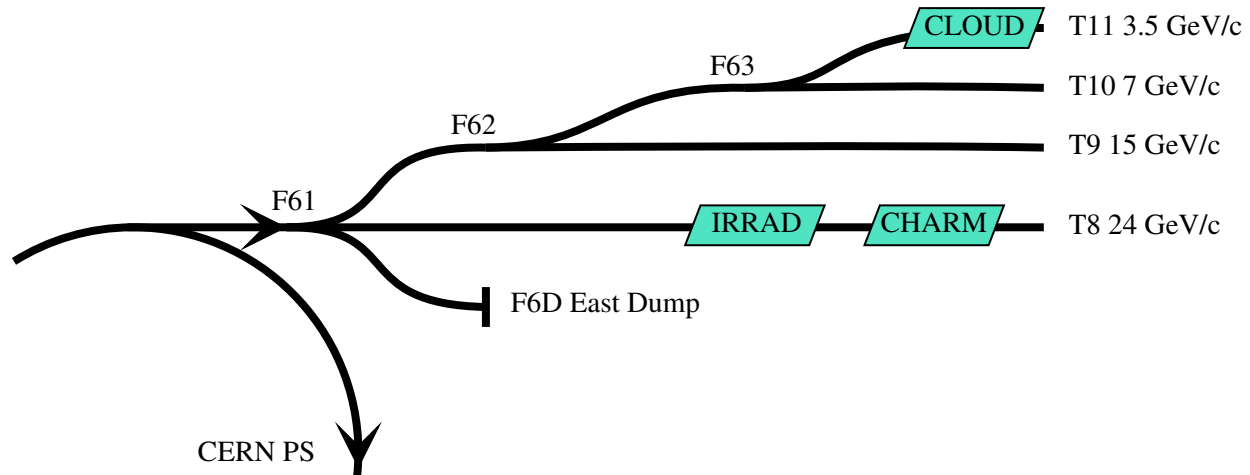


Figure 1.1: Layout diagram of the CERN East Area (EA) beamlines, their proton momenta, and experiments.

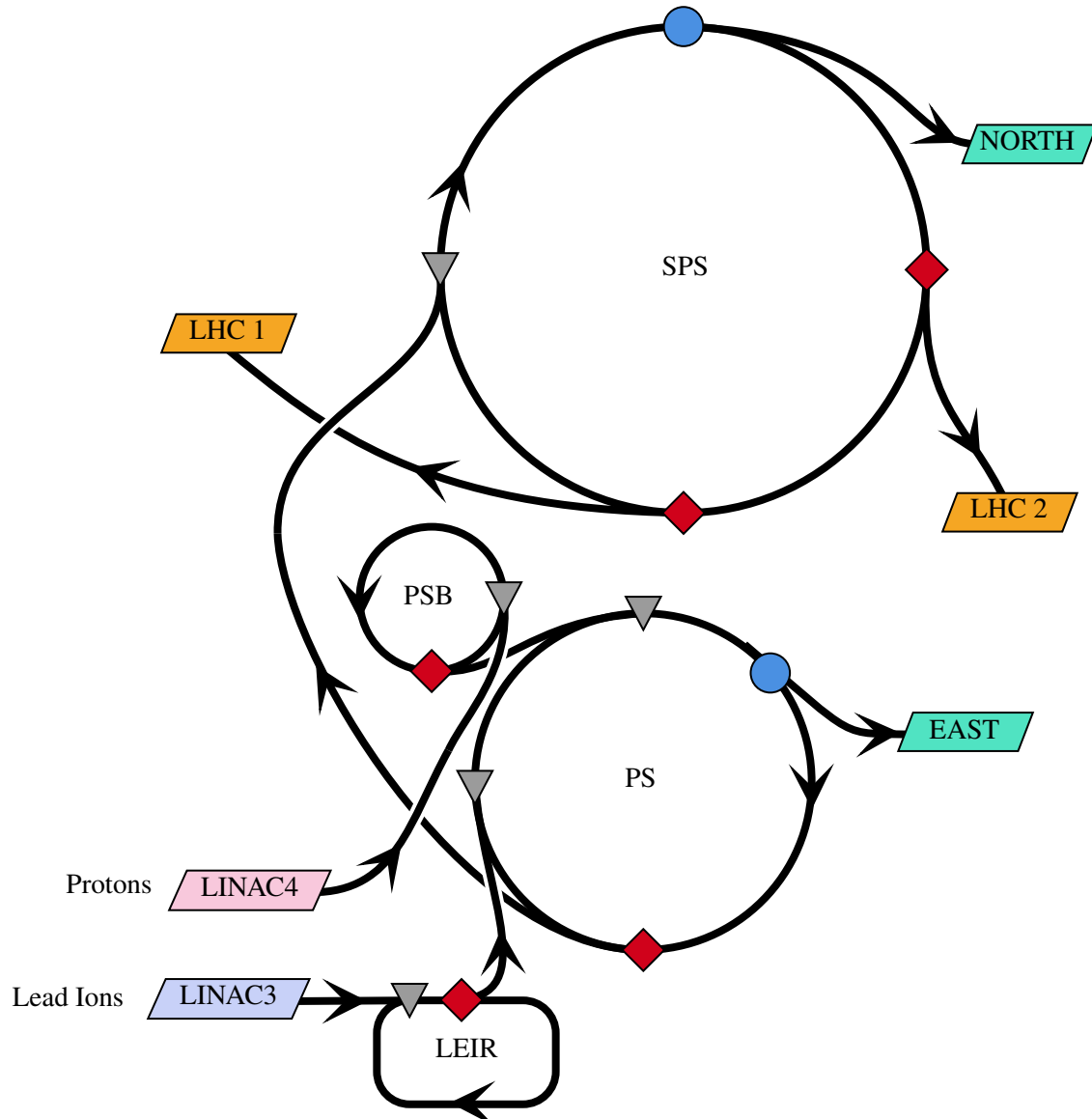


Figure 1.2: Layout diagram of the primary injection chain at CERN. Particles are sourced from either Linac 3 (for Lead ions) or Linac 4 (for Protons), and accelerated through the LEIR or PSB respectively. After injection and acceleration in the PS, beams are extracted either to the SPS or East Area (EA). Particles at the SPS are either extracted at two LHC extraction locations, or towards the North area. Red diamonds mark Fast extraction locations, and blue circles mark Slow extraction regions. Grey triangles mark injection regions.

1.1 Motivation

The CHIMERA experiment, and other experiments located at the East Area and its higher-energy sister site at the SPS North Area, are referred to as fixed-target experiments. These experiments require a semi-continuous flux of particles: if the entire beam of the PS was delivered to a material sample, for example, in an effectively instantaneous “spill” (a controlled removal of particles from the circular accelerator), any sensitive acquisition equipment would become saturated, and the fixed target itself likely destroyed.

At a beam momentum of 5.4 GeV in the PS, the revolution of the beam is around 470 kHz. Therefore, delivering particles over the period of one turn could, at most, provide a spill time on the order of $2\ \mu\text{s}$. This extraction method, known as *fast* extraction, is commonly used to transfer particles between successive accelerators, where the bunched time-structure of the beam must be preserved. To provide spills on the order of $\sim 100\ \text{ms}$ required for these experiments, much longer than the revolution period, a “slow” extraction system is employed.

1.1.1 Extraction Methods

To move particles between consecutive machines along the primary CERN injector chain, the PSB, PS, and SPS are equipped with fast extraction systems. The principles of these processes will be fully explored in the next section, but a general overview and understanding of its benefits and disadvantages can help motivate the use of *slow* extraction.

As previously mentioned, *fast* extraction provides a spill of particles typically over the duration of one turn. A fast magnet, at a suitable location in the machine, imparts a large deflective angle to the beam. This ejects the beam from the nominal orbit, where it encounters a second magnet—called a septum—to deflect the beam into a transfer line. The opposite effect is then used to inject the bunch into the next machine: a magnet “kicks” the particles onto the circulating beam trajectory.

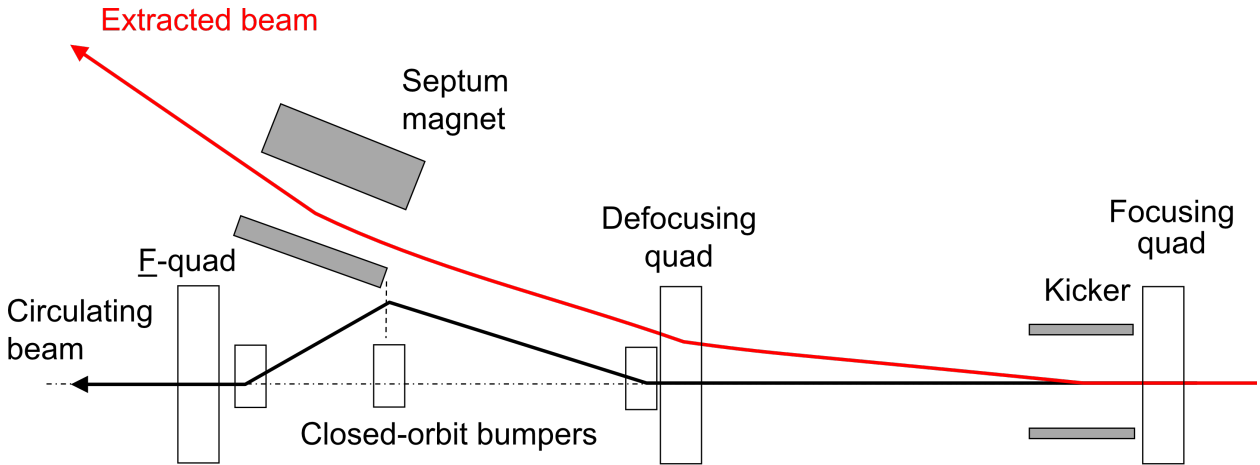


Figure 1.3: Schematic of the general principle of single-turn fast extraction [2].

This method of ***single-turn fast extraction*** (Figure 1.3) is used at two locations in the SPS—Long Straight Sections (LSS) 4 and 6—to fill the two counter-rotating rings in the LHC [2]. The PSB uses the same method, but has the added complexity of “merging” four separate stacked rings to one transfer line [3]. LEIR likewise performs fast extraction [4]. The general layout of these systems are shown in 1.2, where red

diamonds mark fast extraction locations. Fast extraction systems are also used at the beam dump facilities at various stages of the accelerator chain to discard the circulating beam at the SPS and LHC.

In accelerator-to-accelerator contexts, the synchronous nature of fast extraction allows particles to remain bunched. **Multi-turn fast extraction** extends this benefit, and is performed when filling the SPS for its fixed-target experiments (North Area) from the PS. As the SPS (6.9 km) is almost approximately 11 times longer in circumference than the PS¹ (628 m), the entire SPS can be filled by 11 successive extractions of the full PS. This method, coined as *continuous transfer* (CT), introduces the concept of “shaving” the beam with an electrostatic septum. In its current implementation in the PS, the beam is bumped similarly to single-turn fast extraction, but is instead forced over the blade of an electrostatic septum (ES), such that a segment of the beam is ‘sliced’ off, kicked towards a magnetic septum (MS), and extracted. The remaining beam is kicked back onto its orbit. The next turn, the beam has been “rotated” by a quarter turn, and the process repeats, until the finally the remaining core of the beam is bumped directly to the magnetic septum. This provides a spill to the SPS of five bunches over five beam rotations from a single PS bunch.

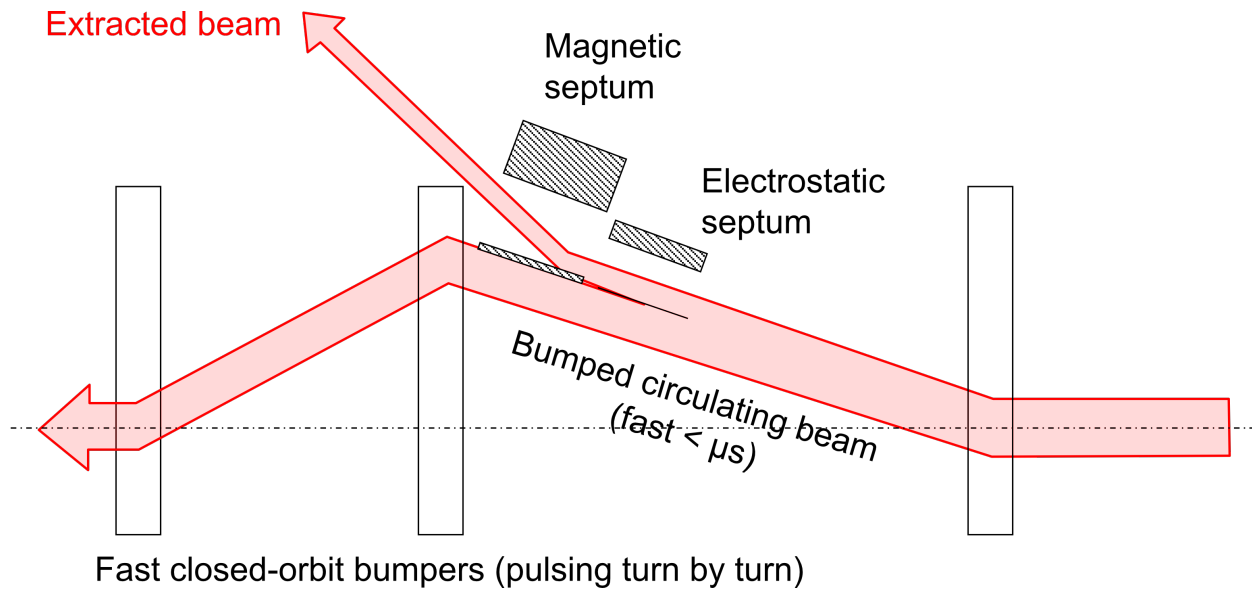


Figure 1.4: Diagram of a general multi-turn fast extraction system [2].

This method of increasing the spill time is, however, limited by the width of the septum blades. As the amount of beam scraped off per turn decreases, the effect of the particles lost on the septum blade increases. To maintain a reasonable extraction efficiency, the beam size would have to become exponentially large.

For example, if a 50% extraction efficiency is desired over 10^4 turns, the beam thickness sliced off by the ES must be the same as the thickness of the blade itself. For the SPS, the ES has blade thickness of $25 \mu\text{m}$. The required diameter of the beam, therefore, would be $2 \cdot 25 \mu\text{m} \cdot 10^4 = 0.5 \text{ m}$. This diameter is already larger than the beam pipes, clearly physically impossible.

In order to provide spills over a longer duration, over many thousands of turns, *slow extraction* must be used.

¹The PS is 100 meters across, and therefore $200\pi\text{m}$

1.1.2 Introduction to Slow Extraction

Slow extraction instead relies on exploiting resonance of the beam as it oscillates around the orbit of the machine. A full theoretical description of these effects will be detailed in chapter 2, but a brief explanation is offered here: the oscillatory motion of a beam can be controlled such that it returns to the same point along the accelerators circumference with the same oscillation phase. The particles will, therefore, travel through the same field of a magnet, and experience the same force on consecutive turns, rapidly becoming unstable.

This resonant effect is usually carefully avoided in particle accelerators. However, with the right configuration, this amplitude growth can be used alongside an ES to separate particles from their orbit, towards an MS, and into the extraction transfer line. Should the effect be slow enough, a small fraction of particles will reach the MS per turns.

The exploitation of resonance to induce extraction is by no means novel; a method akin to slow extraction was first proposed by J. Tuck and L. Teng in 1951 [5], and performed by Le Couteur at the Liverpool cyclotron in 1954 [6]. Many such applications of slow extraction exist, using different effects to drive particles into resonance. This thesis will present some of these methods, particularly focussing on Radio-Frequency Knock-Out slow extraction.

Many medical synchrotrons, such as the MedAustron Synchrotron, use slow extraction to deliver beam to patients for ion beam cancer therapy [7], producing spills of up to 30 s can be produced². In human medical applications, safety is paramount. Therefore, the slow extraction process must be fully understood. Ripples in the intensity of beam have to be carefully controlled in order to provide a steady, predictable irradiation dose to patients.

Small medical synchrotrons are simpler³, newer⁴, and having a far higher operational availability requirement than research accelerators such as the PS. At CERN's PS, however, that benefit cannot be relied upon. Machine time is in high demand, and studies are time-shared between machine development (MD), fixed-target experimental areas, LHC physics injection, and a wide array of other facilities.

Simulations can there provide an important tool in understanding slow extraction spills. New methods can be rapidly developed and tested without requiring extensive (and expensive) machine studies, and wide parameter spaces can be explored to construct functional relationships between input parameters and spill output characteristics.

1.2 Modelling Slow Extraction

subsection 2.1.9 will introduce a mathematical model which can be used to numerically calculate particle trajectories in simple machines. However, with even the simplest of accelerators at CERN containing hundreds of components, computational models quickly become necessary. In addition, slow extraction can operate over many more accelerator turns than other processes, such as fast single-turn injection. In the PS, a spill length of 0.5 s would require approximate 230,000 turns. For even a reasonably powerful machine, these computational simulations quickly become time-consuming.

To aid with the design and construction of CERN's Large Electron-Positron collider (LEP, the predecessor to LHC), the *Methodical Accelerator Design Program* (MAD) [8] was developed. This FORTRAN-based

²Limited to 10 s for patient treatment

³The PS contains 100 bending magnets along its circumference, as opposed to MedAustron's 16

⁴The PS began operation in 1959, and is CERN's oldest accelerator still in operation. MedAustron was first certified in 2016.

scripting tool allowed physicists to define the arrangement and strengths of magnetic elements around an accelerator (the *lattice*), define beam parameters, and calculate the resulting motion of particles (the *optics*). MAD, and its latest version, MAD-X, quickly became the *de facto* standard within CERN’s beam physics community. However, in the twenty years since the release of MAD-X, the landscape of computational accelerator physics has become awash with a wide array of tools, codes, and standards, each with their own specialisations.

Newer tools are introducing improvements such as “ready-to-go” compatibility with General-Purpose Graphical Processing Unit (GPGPU) acceleration. GPUs are specialised hardware capable of performing highly optimised matrix and vector calculations. This makes them ideal for the matrix calculations required for particle accelerator simulations. Additionally, *embarrassingly parallel*⁵ can be run on large number of smaller processing platforms, rather than a single large platform. These platforms could be processing units within a GPGPU, or discrete computer host on a batch-processing network.

⁵A problem which requires minimal no effort to be separated into a large number of independent, concurrently-processed tasks.

Chapter 2

Accelerator Physics Theory

To construct accurate simulations of slow extraction methods, one must first understand the fundamental theory behind particle motion in a circular accelerator. This chapter will introduce the theory required to understand the motion of particles as they travel through an accelerator, and how such oscillatory motion can be exploited to perform slow extraction [9].

2.1 Transverse Beam Dynamics

2.1.1 Coordinate System

The coordinate systems used to describe the dynamic motion of particles in an accelerator such as the PS relies on the periodic nature of a circular accelerator. Using a traditional Cartesian coordinate system would quickly introduce complications when describing circular trajectories, and so a local curvilinear coordinate system is used [10].

The basis vectors for this system, $(\hat{x}, \hat{y}, \hat{s})$, rotate in space as the reference particle moves along the accelerator. The longitudinal vector \hat{s} is tangent to the particle's orbit, and the \hat{x} direction is parallel to the radius of the accelerator. The absolute direction of \hat{y} does not change, but makes one complete rotation in one closed orbit of the reference particle through the accelerator. This system is shown in Figure 2.1, along with the radius of the circular trajectory ρ , and the angle from the origin $s = 0$.

This coordinate system is known as a *Frenet-Serret* coordinate system, and can be rigorously defined by the unit vector *tangent* to the curve \hat{T} (pointing in the direction of motion), the unit vector *normal* to the tangent and on the tangential plane \hat{N} , and the binormal unit vector \hat{B} , the cross product of \hat{T} and \hat{N} . These unit vectors, forming an orthonormal basis spanning \mathbb{R}^3 are equal to the vectors $\hat{x}, \hat{y}, \hat{s}$ by:

$$\begin{pmatrix} \hat{T} \\ \hat{N} \\ \hat{B} \end{pmatrix} = \begin{pmatrix} \hat{s} \\ -\hat{x} \\ \hat{y} \end{pmatrix} \quad \text{Eq. 2.1}$$

The coordinate system $(\hat{x}, \hat{y}, \hat{s})$ relies on the right-hand chirality (Figure 2.2) of the vector cross product for the \hat{x} vector to point radially outwards from the centre of the machine, the \hat{y} vector points upwards, and the \hat{s} vector points in the direction of motion. The direction of \hat{x} to point outwards from the centre of revolution is chosen as injection and extraction line apertures will therefore be located in the positive \hat{x} .

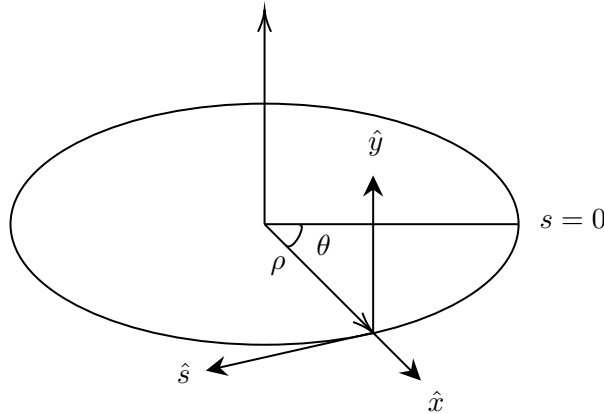


Figure 2.1: The vectors used to define the Frenet-Serret coordinate system.

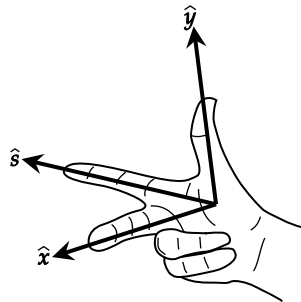


Figure 2.2: The right-hand chirality rule defining the direction of $\hat{x} = \hat{y} \times \hat{s}$

2.1.2 Special Relativity

The equations of motion in this thesis consider particles moving at extremely high velocity, approaching the speed of light c . At CERN, before injection into the PS, particles are accelerated to 2 GeV, and reach 94.8% of the speed of light. At such speeds, relativistic effects are significant.

The Lorentz factor γ is defined as the derivative of *coordinate* time t in the relativistic particle's reference frame, with respect to the *proper* or *lab* time τ in the observer's reference frame. It is calculated as:

$$\gamma = \frac{1}{\sqrt{1 - \frac{v^2}{c^2}}} \quad \text{Eq. 2.2}$$

Also defined is the β factor

$$\beta = \frac{v}{c} \quad \text{Eq. 2.3}$$

and the α factor

$$\alpha = \frac{1}{\gamma} \quad \text{Eq. 2.4}$$

For reasons that will become clear in subsection 2.1.7, these factors will be referred to as $\alpha_c, \beta_c, \gamma_c$.

One important distinction in a relativistic reference frame is the *invariant mass* m_0 versus the relativistic mass m . The invariant mass, or rest mass of any object is the Newtonian mass measured in its own reference

frame. From the *lab* reference frame, this mass is measured as the relativistic mass, defined as

$$m = \gamma m_0 \quad \text{Eq. 2.5}$$

This relativistic mass is conserved just the same as rest mass, and follows the $p = mv$ formula the same as in the rest frame. The rest energy E_0 and *momentum* m_0 are likewise defined in the relativistic frame:

$$E = \gamma m_0 c^2 \quad \text{Eq. 2.6}$$

$$p = \gamma m_0 v \quad \text{Eq. 2.7}$$

For brevity, this report will always assume a relativistic frame, and all mentions of mass m , momentum p , or energy E should be assumed to be relativistic unless otherwise stated.

2.1.3 Particle Variables

Following the basis vectors defining the coordinate system, the following variables are used to characterise the orbit of particles, dependent on s :

In the transverse planes:

- $x(s)$ [m] — the particle's horizontal position with respect to the reference orbit.
- $y(s)$ [m] — the particle's vertical position with respect to the reference orbit.
- $x'(s) = \frac{dx}{ds}$ [rad] — the particle's horizontal angle with respect to the reference orbit.
- $y'(s) = \frac{dy}{ds}$ [rad] — the particle's vertical angle with respect to the reference orbit.

In the longitudinal plane:

- $z = s - s_0$ — the particle's longitudinal position with respect to the reference particle s_0 .
- $\delta = \Delta p/p_0$ — the particle's momentum difference with respect to the reference particle p_0 .

These variables provide 6 vectors fully describing the position of a particle. However, for the remainder of this thesis, the pair of longitudinal variables (z, δ) will be treated separately to the transverse variable pairs (x, x') and (y, y'). This enables a simpler understanding of the effects of beam bending and focussing magnets, as these effects are independent of the longitudinal variables.

2.1.4 Design orbit and Dipoles

An understanding of particle dynamics in an accelerator can be built upon the Lorentz force, describing the force \vec{F} acting on a charged particle with charge q as it moves through an electric field \vec{E} and magnetic field \vec{B} with velocity \vec{v} , given as

$$\vec{F}_{\text{lorentz}} = q \cdot (\vec{E} + \vec{v} \times \vec{B}) \quad \text{Eq. 2.8}$$

This equation can already show why magnetic fields are typically used to bend particles along a circular trajectory and not electric fields; a particle with higher velocity v will experience a greater force from a constant magnetic field \vec{B} , whereas the contribution from the electric field \vec{E} will not benefit from the increasing velocity of a particle.

The other force experienced by a particle in an accelerator is a consequence of conservation of momentum:

$$\vec{F}_{\text{centrif.}} = \frac{m_0 v^2}{\rho} \quad \text{Eq. 2.9}$$

where m_0 is the particle's rest mass, and ρ is the radius of the particle's orbit inside the accelerator.

Equating equations 2.9 and 2.8 yields

$$B\rho = \frac{p}{q} \quad \text{Eq. 2.10}$$

The quantity $B\rho$ is known as the *magnetic rigidity* of a beam, and defines the bending angle of a particle for a given magnetic field.

If the relativistic momentum $p = mv$ of the particle is measured in $\text{GeV}/c_0/\text{amu}$ (atomic mass unit), the magnetic rigidity can be expressed in Tesla-meters:

$$B\rho [\text{T m}] = 3.3356 \cdot p [\text{GeV } c_0^{-1}] \quad \text{Eq. 2.11}$$

Again referring to Equation 2.8 (with the help of Figure 2.2), a magnetic field pointed vertically upwards (along the \hat{y} vector) will cause a positively-charged particle with motion along the \hat{s} vector to experience a bending force along the $-\hat{x}$ direction (illustrated in Figure 2.3). This formulation, however, only considers a single dipole. In reality, the bending magnet structure of accelerators typically consist of multiple dipoles placed around the ring, their power converters connecting in series. The arrangements of these bending magnets—referred to as Main Units (MU) in the context of the PS—will define the reference¹ orbit in the accelerator.

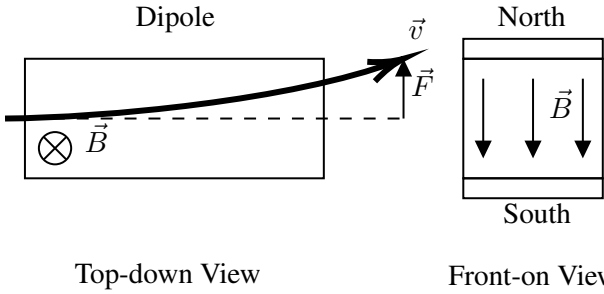


Figure 2.3: A dipole magnet, showing the direction of the magnetic field \vec{B} into the page (left, upwards in front-on view), the current velocity of a positively charged particle \vec{v} , and the Lorentz force \vec{F} , as calculated by $\vec{F} = q\vec{v} \times \vec{B}$

If α is the bending angle of a single MU, then α can be related to the magnetic rigidity by

$$\alpha = \frac{ds}{\rho} = \frac{B ds}{B\rho} \quad \text{Eq. 2.12}$$

Integrating this over all magnets in the ring, therefore, must be equal to one full revolution, 2π

$$\frac{\int B ds}{B\rho} \equiv 2\pi \quad \text{Eq. 2.13}$$

This provides one of the first key insights which is not obvious at first—that “circular” accelerators are in fact more complex shapes, with bending magnets at each vertex, and a *drift* (accelerator sections without

¹Sometimes referred to as *design* orbit

any significant electromagnetic field) or other non-bending multipole magnet at each side: in the case of the LHC, 1,232 dipole magnets are used to keep the beam on its circular path; in the PS—100.

2.1.5 Focussing and Multipoles

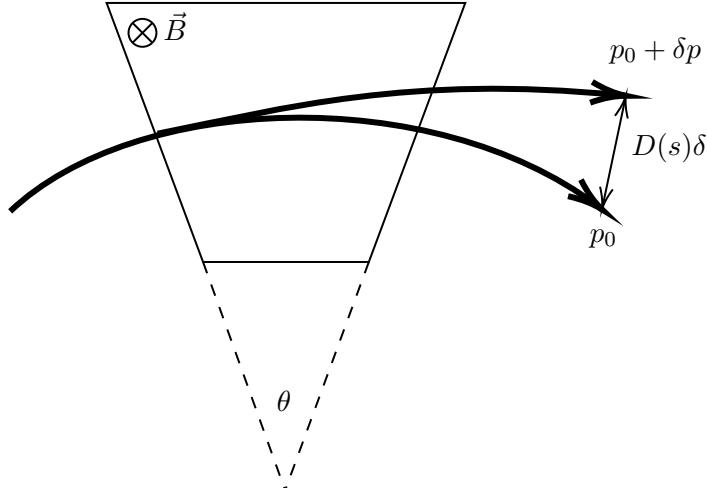


Figure 2.4: A top-down diagram of a sector dipole illustrating how small changes in the beam’s momentum ($\delta = (p - p_0)/p_0$), lead to changes in the bending effect of a dipole, known as dispersion.

Figure 2.4 illustrates the need for corrective elements in the beamline. If a particle is displaced slightly from the design orbit ($x = 0$) or has a variation in momentum (δ) before a dipole element (marked with a downwards magnetic field \vec{B}), the bending effect will differ, and the particle will be displaced from the design orbit after the dipole. This difference in bending effect is known as *dispersion*, and will be analysed in subsection 2.1.8.

To correct for this, synchrotrons use quadrupole elements to “focus” the beam in one transverse plane. An arrangement of four magnetic poles creates a field stronger at higher $|x|$ displacement, causing particles to be pulled back towards the design orbit. However, particles off-axis in the other transverse plane will be pushed further off-axis. To correct for this, a second quadrupole is placed further along in the beamline, with the magnetic poles arranged in the opposite orientation. This arrangement, known as a FODO lattice, is shown in Figure 2.5 (right).

Sextupoles—third order magnets—provide additional correction to the beam. Depicted in Figure 2.6, these can be understood by expanding on the optical analogy used thus far, where the Dipole takes the role of a prism, bending the light. As with prisms, beams with higher energy are bent less than low energy, and so the component wavelengths (or energies) in the beam beam are dispersed. The sextupole is analogous to an aspherical element, correcting for chromatic aberration introduced by the focussing quadrupole. Again, as with its optical analogue—a focussing lens—the quadrupole has shorter focal length for higher energy particles. The sextupole acts as a focussing lens at high energy and diverging lens at low energy, correcting for this chromatic effect.

Now that the basic magnetic elements have been introduced, and an understanding of the beam’s momentum p has been formed, we can redefine our transverse coordinates in terms of momentum: $p_x = x' \cdot p$ and $p_y = y' \cdot p$ now define our transverse coordinates. These coordinates will allow us to build a picture of the multi-particle transverse dynamics of the beam.

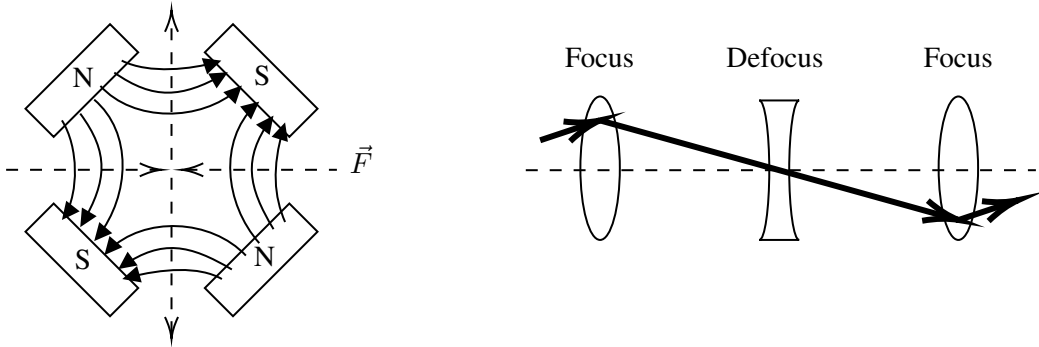


Figure 2.5: Diagram (left) showing the field of a *normal* oriented quadrupole, providing focussing in x but defocussing in y . The force experienced by a positively-charged particle is shown as dashed arrows. Right-hand diagram illustrates a FODO cell.

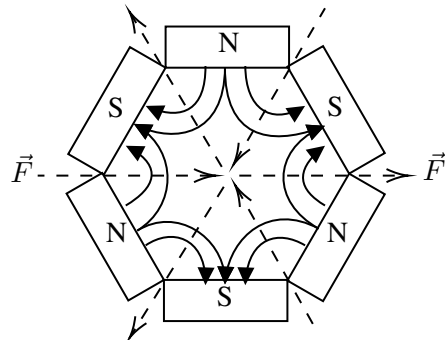


Figure 2.6: A diagram showing the field of a *normal* oriented sextupole. The force experienced by a positively-charged particle is shown as dashed arrows.

2.1.6 Single-Particle Oscillatory Motion

In a periodic (circular) accelerator, the linear equation for transverse motion takes the form of a differential equation:

$$x'' - x \cdot \left(k - \frac{1}{\rho^2} \right) = 0 \quad \text{Eq. 2.14}$$

where x is the transverse displacement as a function of longitudinal position s , and k is the quadrupole focussing coefficient, defined as

$$k = \frac{q}{p} \cdot \frac{dB_y}{dx} \quad \text{Eq. 2.15}$$

The $1/\rho^2$ term represents the effect of the dipole bending field, providing a weak focussing effect. If we enforce the periodicity² in s of k , Equation 2.14 can be rewritten in a compact form

$$x''(s) - \tilde{k}(s)x(s) = 0 \quad \text{Eq. 2.16}$$

where the quadrupole focussing component $\tilde{k}(s)$ is now a function of s .

This equation can be physically understood with another analogous example: one where the weak focussing effect of the dipoles are modelled as the curved sides of a toroidal, akin to a circular gutter

²i.e. that the quadrupoles do not change between consecutive revolutions

pipe, illustrated in 2.7. The weak focussing effect creates harmonic motion for particles not on the ideal zero-amplitude path. This describes how the harmonic motion, described by Equation 2.16, relates to motion around an ideal orbit.

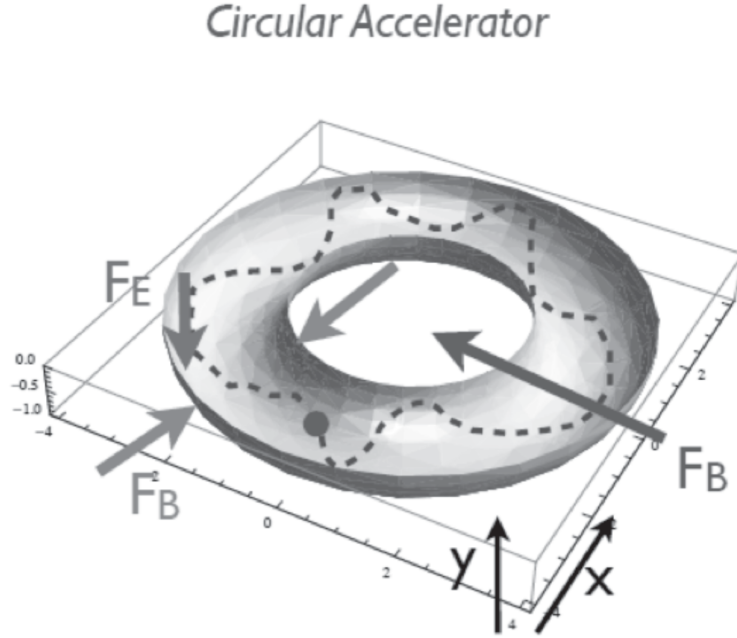


Figure 2.7: A diagram showing the analogy between the transverse motion of a particle in a circular accelerator and a ball rolling in a circular gutter.

With the given periodic boundary condition $\tilde{k}(s + L) = \tilde{k}(s)$, 2.16 is known as the Hill's equation.

Following Floquet's theorem [11], general solution to this equation takes the form of

$$x(s) = \sqrt{\varepsilon} \sqrt{\beta(s)} \cos(\varphi(s) - \varphi_0) \quad \text{Eq. 2.17}$$

where ε and φ_0 are integration constants characterising the initial conditions of the particle, and $\beta(s)$ and $\varphi(s)$ are the amplitude and phase functions (respectively) of the oscillation.

The β twiss function must also satisfy the periodic constraint $\beta(s + L) = \beta(s)$, and is related to the φ phase function by the following equation:

$$\varphi(s) = \int_0^s \frac{ds}{\beta(s)} \quad \text{Eq. 2.18}$$

Taking the derivative of Eq. 2.17 with respect to s gives an equation for the angle of the trajectory:

$$x'(s) = \sqrt{\varepsilon} \sqrt{\beta(s)} \left(\frac{1}{2} \beta'(s) \cos(\varphi(s) - \varphi_0) + \sin(\varphi(s)) \right) \quad \text{Eq. 2.19}$$

A basic analysis of Eq. 2.18 shows that at locations with large β amplitude (and thus a large transverse displacement), phase advance φ is small, and vice versa. The overall phase advance of transverse oscillations

over one revolution of 2π is known as the *betatron tune* of the accelerator, and is defined as

$$Q = \frac{1}{2} \oint \frac{ds}{\beta(s)} \quad \text{Eq. 2.20}$$

This quantity, often simply referred to as *tune*, effectively indicates how many complete transverse oscillations a particle makes in one turn. The fractional part of this value is the most significant, and often a tune will be reference to the integer part; a tune of $Q = 6.\dot{3} = 19/3$ is, for the purposes of this thesis, equivalent to $Q = 1/3$.

The final quantity of interest from these expressions is an effect of non-linearities in quadrupoles. Particles with momentum different to the reference particle p_0 will experience different focussing effects in quadrupoles. This slight change in focussing will effect the oscillatory motion of off-momentum particles, and result in a spread of tunes throughout a distribution of particles. The variation of this tune, with respect to the variation in momentum, is characterised by the *chromaticity*, variously defined as Q' or η :

$$Q' = \frac{\delta Q/Q}{\delta p/p} \quad \text{Eq. 2.21}$$

A machine with non-zero chromaticity will necessarily have a tune spread, which can be controlled with the use of sextupoles.

2.1.7 Phase Space

Equation 2.17 and Equation 2.19 introduced an integration constant ε , which is a characteristic parameter of the particle or ensemble of particles. It is known as (transverse) emittance, and is usually considered with particle ensembles in mind. These two equations can be manipulated to provide an expression for ε :

$$\varepsilon = \gamma(s)x^2(s) + 2\alpha x(s)x'(s) + \beta(s)x'^2(s) \quad \text{Eq. 2.22}$$

where

$$\alpha(s) = -\frac{1}{2} \frac{d\beta(s)}{ds} \quad \text{Eq. 2.23}$$

and

$$\gamma(s) = \frac{1 + \alpha^2(s)}{\beta(s)} \quad \text{Eq. 2.24}$$

These further two constants, along with β , form the *Courant-Snyder Parameters* [12], commonly referred to as the *twiss parameters*³.

These parameters can be readily understood in the *phase space*⁴ of (x, x') . Illustrated in Figure 2.8, Equation 2.22 describes an ellipse, which covers the area of the particle ensemble in phase space. The area of this ellipse is given by $\pi \cdot \varepsilon$, and may be interchangeably defined as the emittance.

Liouville's theorem states that, under conservative forces, this emittance is conserved, and no external field can change it, and hence Equation 2.17 provides it as an invariant of motion.

³Even Richard Q. Twiss, a British astronomer, was himself unsure as to how the parameters became attributed to him [13].

⁴This is opposed to the more formal phase space (x, p_x) , which does not provide these insights as succinctly.

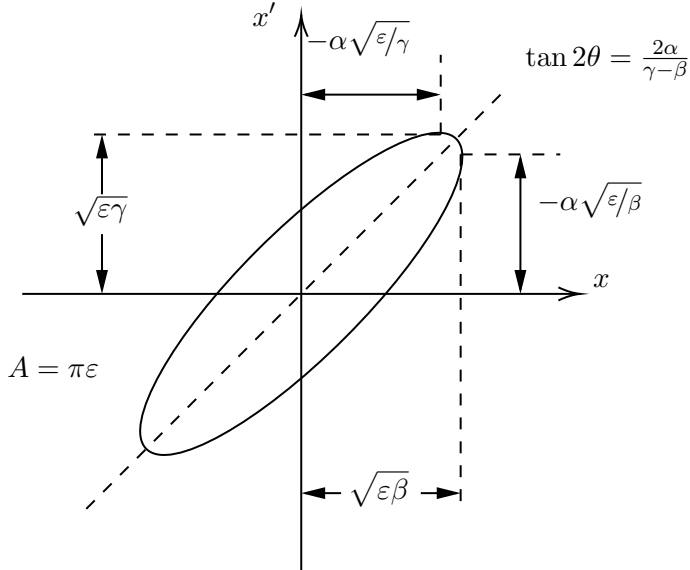


Figure 2.8: Phase space in (x, x') showing the ellipse formed by a particle, and its relation to the Twiss parameters.

2.1.8 Dispersion

We now consider the oscillatory motion of *multiple* multi-energetic particles, with reference to the ideal particle. This ideal particle, with momentum p_0 and initial conditions all equating to zero, has a path through the field centre of all quadrupoles, and so experiences no quadrupole effect k . This means that its motion is controlled by the weak dipole focussing $1/\rho^2$. A nominal particle, still with momentum p_0 but with initial displacement and/or angle conditions, will perform closed-loop betatron oscillations around this path.

A particle with a momentum offset, $\Delta p = p - p_0 > 0$, will still satisfy 2.14 from before, but the inhomogeneous form

$$x''(s) - x \left(k - \frac{1}{\rho^2} \right) = \frac{1}{\rho} \frac{\Delta p}{p_0} \quad \text{Eq. 2.25}$$

We can use the homogenous solution previously found to form the complete solution $x(s) = x_h(s) + x_i(s)$. This inhomogeneous term $x_i(s)$, is normalised by the momentum difference to produce the Dispersion function

$$D(s) = \frac{x_i(s)}{\Delta p/p_0} \quad \text{Eq. 2.26}$$

describing how the additional amplitude of an off-momentum particle depends on the momentum difference. This dispersion function satisfies, for the circumference of the machine:

$$D'' - D \left(x - \frac{1}{\rho^2} \right) = \frac{1}{\rho(s)} \quad \text{Eq. 2.27}$$

2.1.9 Matrix Formalism

Outside of the context of periodic boundary conditions, Equation 2.17 and Equation 2.19 can be solved by imposing initial conditions x_0 and x'_0 :

$$x(s) = x_0 \cos(\sqrt{K} \cdot s) + \frac{x'_0}{\sqrt{K}} \sin(\sqrt{K} \cdot s) \quad \text{Eq. 2.28}$$

$$x'(s) = -x_0 \sqrt{K} \sin(\sqrt{K} \cdot s) + x'_0 \cos(\sqrt{K} \cdot s) \quad \text{Eq. 2.29}$$

where K now defines the quadrupole focussing effect k (Equation 2.15) and the dipole weak focussing effect:

$$K = \frac{1}{\rho^2} - k \quad \text{Eq. 2.30}$$

These two equations can be written as a matrix equation:

$$\begin{pmatrix} x \\ x' \end{pmatrix} = \mathbf{M} \begin{pmatrix} x_0 \\ x'_0 \end{pmatrix} \quad \text{Eq. 2.31}$$

where \mathbf{M} is the transfer matrix

$$\mathbf{M} = \begin{pmatrix} \cos(\sqrt{K} \cdot s) & \frac{1}{\sqrt{K}} \sin(\sqrt{K} \cdot s) \\ -\sqrt{K} \sin(\sqrt{K} \cdot s) & \cos(\sqrt{K} \cdot s) \end{pmatrix} \quad \text{Eq. 2.32}$$

The definition of this transfer matrix \mathbf{M} can be expanded to define the variety of magnets used in an accelerator. In the simple case, where no magnet is present, we define the transfer matrix for a drift space of length L :

$$\mathbf{M}_{\text{drift,x}} = \mathbf{M}_{\text{drift,y}} = \begin{pmatrix} 1 & L \\ 0 & 1 \end{pmatrix} \quad \text{Eq. 2.33}$$

For a normal dipole magnet bending only horizontally, where $k = 0$ and $K_x = 1/\rho^2$, the transfer matrix is:

$$\mathbf{M}_{\text{dipole,x}} = \begin{pmatrix} \cos\left(\frac{L}{\rho}\right) & \rho \sin\left(\frac{L}{\rho}\right) \\ -\frac{\sin\left(\frac{L}{\rho}\right)}{\rho} & \cos\left(\frac{L}{\rho}\right) \end{pmatrix} \quad \text{Eq. 2.34}$$

$$\mathbf{M}_{\text{dipole,y}} = \mathbf{M}_{\text{drift,y}} \quad \text{Eq. 2.35}$$

For a normal quadrupole, where $K_x = -k$ and $K_y = k$, the transfer matrix is:

$$\mathbf{M}_{\text{quad,x}} = \begin{pmatrix} \cos(\sqrt{-k} \cdot L) & \frac{1}{\sqrt{-k}} \sin(\sqrt{-k} \cdot L) \\ -\sqrt{-k} \sin(\sqrt{-k} \cdot L) & \cos(\sqrt{-k} \cdot L) \end{pmatrix} \quad \text{Eq. 2.36}$$

$$\mathbf{M}_{\text{quad,y}} = \begin{pmatrix} \cos(\sqrt{k} \cdot L) & \frac{1}{\sqrt{k}} \sin(\sqrt{k} \cdot L) \\ -\sqrt{k} \sin(\sqrt{k} \cdot L) & \cos(\sqrt{k} \cdot L) \end{pmatrix} \quad \text{Eq. 2.37}$$

If we define the properties of each element in the accelerator (the lattice), we can then define the transfer matrix for the entire accelerator as the product of the transfer matrices of each element. For example, a FODO

lattice with an initial bending dipole can be defined as:

$$M_{\text{total}} = M_{\text{dipole}} + M_{\text{quad}} + M_{\text{drift}} - M_{\text{quad}} + M_{\text{drift}} + \dots \quad \text{Eq. 2.38}$$

This is the principle by which *particle tracking codes*, such as MAD-X, operate. An input lattice file defines the structure and properties of the magnets composing the accelerator, and particle variables are then computed with matrix multiplication.

2.1.10 Normalised Phase Space

Expanding on the idea of matrix formalism and the phase space ellipse, many particle tracking codes operate in *normalised* phase space (x_n, x'_n) —that is, where the phase space of (x, x') is linearly transformed in a way which results in the phase space ellipse becoming circular. The matrix transformation is therefore defined as

$$\begin{pmatrix} x \\ x' \end{pmatrix} = \begin{pmatrix} \frac{1}{\sqrt{\beta_x}} & 0 \\ \frac{\alpha_x}{\sqrt{\beta_x}} & \sqrt{\beta_x} \end{pmatrix} \begin{pmatrix} x_n \\ x'_n \end{pmatrix} \quad \text{Eq. 2.39}$$

2.2 Longitudinal Dynamics

Where the transverse planes principally consider bending and focussing effects from magnetic fields, the longitudinal plane considers acceleration effects from RF fields. Returning again to Equation 2.8, we instead now consider the *electric* component:

$$\vec{F} = q\vec{E} = \frac{dp}{dt} \quad \text{Eq. 2.40}$$

An electric field of magnitude E_0 travelling in the s direction can be defined as

$$E_s = E_0 \cos(\omega_{RF}t) \quad \text{Eq. 2.41}$$

where ω_{RF} is the RF frequency. Therefore, for a synchronous particle with synchronous phase ϕ_s , the rate of energy gain is

$$\frac{dE_s}{ds} = eE_0 \sin \phi_s \quad \text{Eq. 2.42}$$

In a synchrotron, where the orbit of particles is of constant radius, the magnetic field B needs to increase in time (*ramp*) as the particle is accelerated. Additionally, to keep the particle in phase with the RF cavity, the frequency of the RF ω_{RF} must follow the particle's energy gain. This synchronous condition, for velocities $v \ll c$, is defined as

$$\frac{2\pi\rho}{v_s} = \frac{h}{\omega_{RF}} \quad \text{Eq. 2.43}$$

where h is the RF harmonic, the number of RF cycles per revolution. For East Area beams in the PS, $h = 8$ acceleration is used. This means that there are eight stable “particles”, spread equidistantly around the ring circumference.

2.2.1 Magnetic Ramping

To keep a particle with increasing energy bent along a path of constant radius, the magnetic field B of the bending dipoles must increase as RF acceleration occurs. Recalling Equation 2.10, and deriving by time,

obtains

$$\frac{dp}{dt} = q\rho\dot{B} \quad \text{Eq. 2.44}$$

For one turn in a synchrotron, this results in a momentum gain

$$\Delta p_{rev} = q\rho\dot{B}T_{rev} = \frac{Lq\rho R\dot{B}}{v} \quad \text{Eq. 2.45}$$

where L is the machine length.

Recalling ??, $\Delta E = v\Delta p$, and so the energy gain per revolution is

$$\Delta E_{rev} = Lq\rho R\dot{B} = qV \sin \phi_s \quad \text{Eq. 2.46}$$

where ϕ_s is the synchronous phase. This stable phase therefore changes while energy is ramped:

$$\phi_s = \arcsin \left(L\rho \frac{\dot{B}}{V_{RF}} \right) \quad \text{Eq. 2.47}$$

The RF frequency must also ramp as particles increase in energy, and revolution frequency increases. From the earlier definition $\omega_{RF} = \omega h$:

$$\frac{f_{RF}}{h} = f_{rev} = \frac{v}{2\pi R} = \frac{1}{2\pi} \frac{qc^2}{E} \frac{\rho}{R} B \quad \text{Eq. 2.48}$$

2.2.2 Dispersion

Next, akin to subsection 2.1.8, we consider small perturbations in momentum with respect to an ideal path. We define two parameters:

$$\alpha_p = \frac{\Delta L/L}{\Delta p/p} \quad \text{Eq. 2.49}$$

where α_p , the *momentum compaction factor*, is distinct from the relativistic α_c and Twiss parameter α .

$$\eta = \frac{\Delta f_{rev}/f_{rev}}{\Delta p/p} \quad \text{Eq. 2.50}$$

where η , the *slip factor*, is the relative change of revolution frequency with momentum.

Using the dispersion function Equation 2.26, we can relate the momentum compaction factor to its effect on orbit length s_0 [14, 5.1]

$$\alpha_c = \frac{1}{L} \int \frac{D_x(s)}{\rho(s)} ds_0 \quad \text{Eq. 2.51}$$

Using the revolution frequency⁵ $f_{rev} = \beta_c c / 2\pi R$, we define the relative revolution frequency change Δf_{rev} as

$$\Delta f_{rev} = \frac{d\beta_c}{\beta_c} - \frac{dR}{R} = \frac{d\beta_c}{\beta_c} - \alpha_c \frac{dp}{p} \quad \text{Eq. 2.52}$$

This defines a *transition energy* γ_{tr} such that $\eta = 0$, causing no change in revolution frequency f_{rev} for a small momentum change Δp :

$$\gamma_{tr} = \frac{1}{\sqrt{\alpha_c}} \quad \text{Eq. 2.53}$$

⁵NB: β_c here refers to the relativistic Lorentz factor v/c

Above this transition energy, where $\eta < 0$, the particle has velocity $v \rightarrow c$, and so the path-length change dominates the velocity change. This is the standard configuration of accelerators. Below this transition energy, where $\eta > 0$, the increase of velocity is significantly larger than the path-length change effect. At this transition energy, both effects compensate, and so f_{rev} becomes independent of Δp . Here, the *synchrotron* longitudinal oscillations stop, and particles not on the synchronous phase ϕ_s will rapidly gain energy, and become lost due to dispersion D .

2.2.3 Longitudinal Phase Space

These effects can be analysed by considering phase space coordinates—this time in the longitudinal plane. This space is constructed with variables $(\phi, \Delta p/p)$, and shown in Figure 2.9. A full derivation for the longitudinal motion invariants can be found in [14], where the synchronous phase ϕ_s defines the orbit with zero longitudinal oscillation. Outside of the stable envelope, demarcated by the *separatrix*, particles are lost to instability. The region within the separatrix is known as the *RF bucket*, and the area occupied by stable particles, the *RF emittance*.

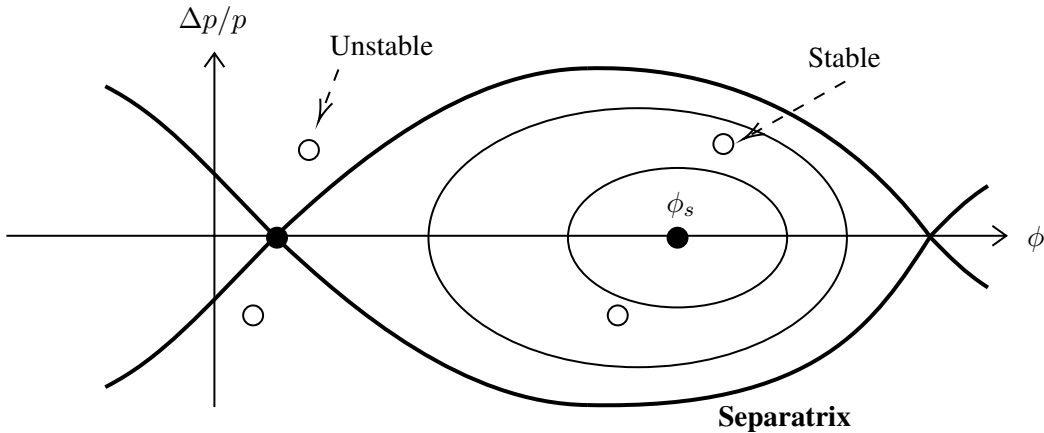


Figure 2.9: Longitudinal Phase Space, showing particles at the synchronous phase ϕ_s , inside stability, and in unstable motion. The separatrix, bold, separates these two regions.

2.3 Slow Extraction

Now that the fundamentals of accelerator beam physics are established, this section will introduce the principles behind *slow extraction* (SX). Various methods of performing SX will be covered, but the particular method covered in this thesis—*Radio-Frequency Knock-Out* (RFKO)—will be described in detail.

2.3.1 Sextupoles and $1/3$ -Integer Resonance

subsection 2.1.8 introduced the concept of dispersion in reference to a multi-energetic beam. A simplified mono-energetic accelerator model can be constructed using only dipoles and quadrupoles, but dispersive effects require the use of sextupole magnets. The transverse field of a sextupole magnet has the form

$$B_x = -6B_3 xy \quad \text{Eq. 2.54}$$

$$B_y = -3B_3(x^2 - y^2) \quad \text{Eq. 2.55}$$

where

$$B_3 = -\frac{1}{6} \left(\frac{d^2 B_y}{dx^2} \right)_0 \quad \text{Eq. 2.56}$$

Taylor Expansion? In *normalised* coordinates (subsection 2.1.10), these effect of these fields (in a thin-lens approximation) becomes

$$\begin{aligned} \Delta x &= 0 & \Delta x' &= S(x^2 - \frac{\beta_y}{\beta_x} y^2) \\ \Delta y &= 0 & \Delta y' &= -2S \frac{\beta_y}{\beta_x} xy \end{aligned}$$

where S , the normalised sextupole strength, is

$$S = \frac{1}{2} \beta_x^{2/3} l_s k' \quad \text{Eq. 2.57}$$

where l_s is the sextupole equivalent length, and k' is the normalised sextupole field:

$$k' = -6 \frac{B_3}{B\rho} \quad \text{Eq. 2.58}$$

For horizontal transverse extraction, such as will be studied in this thesis, the vertical y component of the sextupole field is neglected, as the ratio on which it depends, β_y/β_x , is vanishingly small: the amplitude of oscillations in the vertical plane is significantly less than in horizontal.

Recalling the matrix formalism established in subsection 2.1.9, we use a general transfer matrix for n turns with a betatron tune Q :

$$\mathbf{M}_n = \begin{pmatrix} \cos(2\pi n Q_x) & \sin(2\pi n Q_x) \\ -\sin(2\pi n Q_x) & \cos(2\pi n Q_x) \end{pmatrix} \quad \text{Eq. 2.59}$$

The tune of a particle is then defined as a third-integer, i.e.

$$Q_x = i \pm 1/3 + \delta Q, \quad i \in \mathbb{Z}, |\delta Q| \ll 1/3 \quad \text{Eq. 2.60}$$

The tune distance, δQ , is therefore the distance of the particle from the resonance. The n -turn matrix can then be approximated for *modulo-3* turns:

$$\begin{pmatrix} x \\ x' \end{pmatrix}_1 = \begin{pmatrix} -1/2 & \pm\sqrt{3}/2 \\ \mp\sqrt{3}/2 & -1/2 \end{pmatrix} \begin{pmatrix} x \\ x' \end{pmatrix}_0 \quad \text{Eq. 2.61}$$

$$\begin{pmatrix} x \\ x' \end{pmatrix}_2 = \begin{pmatrix} -1/2 & \mp\sqrt{3}/2 \\ \pm\sqrt{3}/2 & -1/2 \end{pmatrix} \begin{pmatrix} x \\ x' \end{pmatrix}_0 \quad \text{Eq. 2.62}$$

$$\begin{pmatrix} x \\ x' \end{pmatrix}_3 = \begin{pmatrix} 1 & 6\pi \cdot \delta Q \\ -6\pi \cdot \delta Q & 1 \end{pmatrix} \begin{pmatrix} x \\ x' \end{pmatrix}_0 \quad \text{Eq. 2.63}$$

Therefore, a particle with $\delta Q = 0$, i.e. exactly on resonance, will return to its original position after three turns. For such a particle, the change in normalised position x and divergence x' from initial conditions (x_0, x'_0) after three turns is therefore calculated as

$$\Delta x_3 = \mu x'_0 + \frac{2}{3} S x_0 x'_0 \quad \text{Eq. 2.64}$$

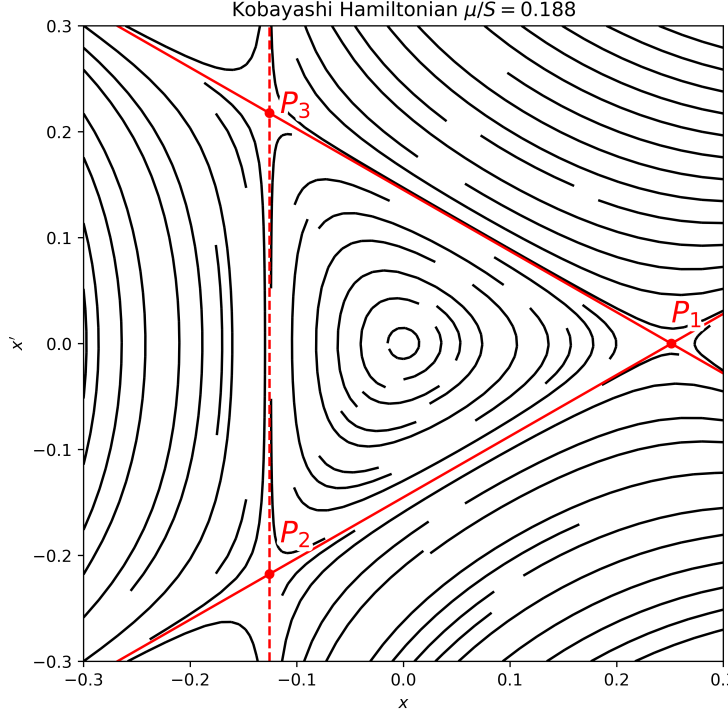


Figure 2.10: Normalised phase-space map of the Kobayashi Hamiltonian, for a ratio $\mu/S = 0.188$. The points P_1, P_2, P_3 are shown, with connecting lines.

$$\Delta x'_3 = -\mu x_0 + \frac{3}{4}S(x_0^2 - x_0'^2) \quad \text{Eq. 2.65}$$

where μ , the *modified tune distance*, is defined as $\mu = 6\pi \cdot \delta Q$, and S is the normalised sextupole strength (Equation 2.57).

The values of Δx_3 and $\Delta x'_3$ are known as the *spiral step* and *spiral kick*. The *Hamiltonian* is now used to analyse this motion in phase-space. The Hamiltonian, \mathbf{H} is a time-independent constant of motion, the contours of which describe the *phase-space map*, the motion of a particle in normalised phase-space. Assuming the 3-turn time is small enough to be continuous, the *Kobayashi Hamiltonian* [15] is defined as

$$\mathbf{H} = \frac{\mu}{2}(x^2 + x'^2) + \frac{S}{4}(3xx'^2 - x^3) \quad \text{Eq. 2.66}$$

The first term describes the typical circular phase-space motion familiar from subsection 2.1.7, with a sextupole strength $S = 0$ (i.e. a linear machine). The second term describes the sextupole effect, transforming the elliptical map into a triangular trajectory for increasing values of x and x' . The phase-space map is shown in Figure 2.10. A boundary triangle is easily identified from the map, which defines the trajectory of the stable particle with greatest possible amplitude, before the motion becomes unstable. Outside of this stable region, the particle trajectories do not close on themselves, and the particle will rapidly gain amplitude. The region bounded by this *separatrix* is known as the *acceptance* the size of which is defined by $|\mu/S|$, and can

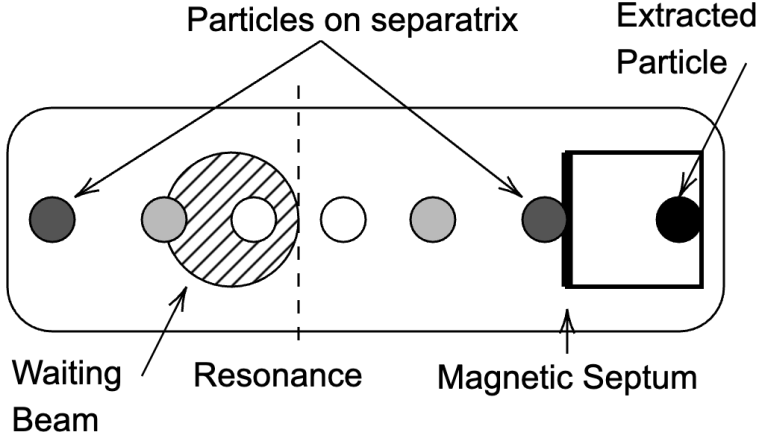


Figure 2.11: A real-world diagram of momentum-driven slow extraction, looking along the s direction at the magnetic septum location. The waiting beam approaches resonance (dashed), and some particles begin large turn-by-turn oscillations (increasing shaded gradient with turn number) before they jump the septum blade (thick black line) and will be extracted.

be found by factorising \mathbf{H} at a value of $(2\mu/3)^3/S^2$, which factorises to three points:

$$P_1 = \left(\frac{4}{3} \frac{\mu}{S}, 0 \right) \quad \text{Eq. 2.67}$$

$$P_2 = \left(-\frac{2}{3} \frac{\mu}{S}, -\frac{2\mu}{\sqrt{3}S} \right) \quad \text{Eq. 2.68}$$

$$P_3 = \left(-\frac{2}{3} \frac{\mu}{S}, \frac{2\mu}{\sqrt{3}S} \right) \quad \text{Eq. 2.69}$$

The x location of the stable particle, h can also be defined as

$$h = \frac{2}{3} \frac{\mu}{S} = \frac{4\pi}{S} \delta Q \quad \text{Eq. 2.70}$$

Therefore, the lines connecting P_1, P_2 and P_1, P_3 (solid lines in Figure 2.10), along with the vertical line at $-h$ (dashed line in Figure 2.10), define the separatrix. The acceptance, the area bounded by the separatrices, is defined as $A = 3\sqrt{4}h^2$.

2.3.2 Slow Extraction Principles

The fundamental principle of slow extraction exploits the unstable boundary created by sextupolar fields. After a beam is injected and stable, this *waiting beam* is accelerated towards the $1/3$ -integer resonance. A particle at resonance will then “lock on” to one of the separatrix arms, and its amplitude will grow in steps of three turns, rotating around the three separatrices. By carefully controlling the rate at which particles enter resonance, the 3-turn amplitude growth (spiral step) can be adjusted to create a desired flux of particles entering resonance. After a number of turns of amplitude growth (typically hundreds), an electrostatic septum located at some distance from the waiting beam will provide a kick necessary to extract the particles. A real-world diagram of slow extraction is shown in Figure 2.11.

There are a variety of methods to provide acceleration of the beam towards resonance, which fall into two categories: *momentum-driven* methods rely on accelerating the beam towards a stationary resonance by

controlling the momentum $\Delta p/p$, whereas *amplitude-driven* methods use transverse noise or RF excitation at the beam's revolution frequency to create increasing betatron amplitudes.

Other methods involve moving the resonance itself, by changing the tune of the machine. This can be accomplished by using quadrupoles (probably the first and simplest method devised) or sextupoles, but is rarely due to an array of complications arising from the changing transverse optics. Implementations would require active compensation to maintain the beam's position, size, and ultimately stability. Quadrupole-driven extraction is, additionally, highly sensitive to power-supply ripples—residual variation in the voltage/current produced by AC-DC power converters.

These categories are not mutually exclusive, and some of the methods discussed will use a combination of effects to achieve slow extraction.

2.3.3 Steinbach Diagram

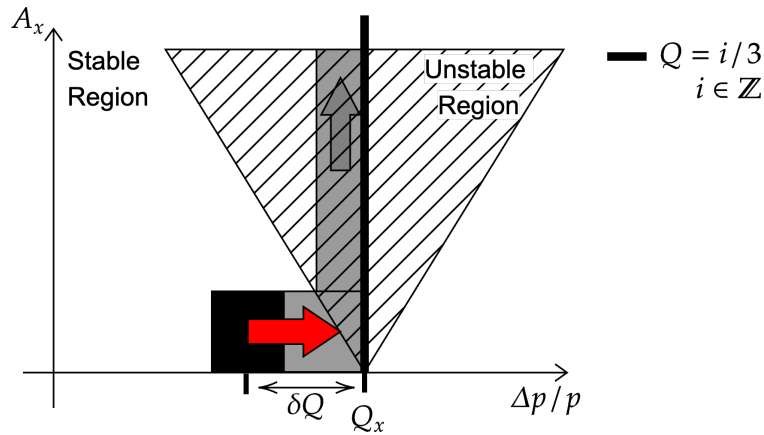


Figure 2.12: Stienbach diagram of momentum-driven slow extraction. Waiting beam in black, resonance driving effect in red, unstable beam in grey.

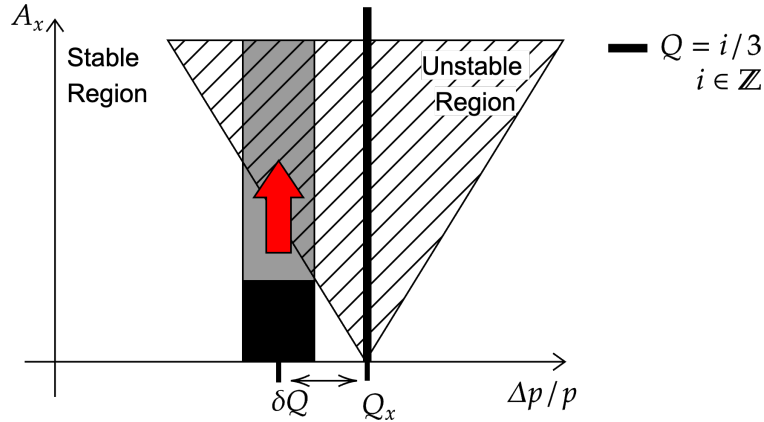


Figure 2.13: Stienbach diagram of amplitude-driven slow extraction. Waiting beam in black, resonance driving effect in red, unstable beam in grey.

The two beam-moving methods of momentum- and amplitude-driven slow extraction can be compared using a Stienbach⁶ diagram. This plots the beam amplitude A_x as a function of momentum $\Delta p/p_0$. The

⁶Attributed to C. Steinbach, CERN

sextupole instability is shown as a triangle, within which is the unstable region beyond the phase-space map separatrices. Figure 2.12 and Figure 2.13 illustrate *momentum* and *amplitude* driven slow extraction respectively. In order for a particle to be considered stable, its single-particle emittance ϵ must be lower or equal to the area of the separatrix triangle. Using Equation 2.70, this condition is expressed as

$$A^2\pi \leq \frac{48\sqrt{3}\pi}{S^2} \delta Q^2\pi \quad \text{Eq. 2.71}$$

If this condition is plotted on a (Q, A) graph, the stable triangle shown in Figure 2.12 and Figure 2.13 is seen. The width of this unstable triangle, known as the *stopband*, is proportional to S .

2.3.4 Slow Extraction Methods

Betatron Core

A simple treatment of momentum-driven slow extraction is through the use of a *betatron core*. Used by accelerators such as the *National Center for Oncological Hadrontherapy* [16] (CNAO) and MedAustron [17], a betatron core is a circular magnet placed around the beam to produce a longitudinal voltage along s . Both the CNAO and MedAustron designs, and many more medical machines, were based on a landmark report *Proton-Ion Medical Machine Study* [18] (PIMMS), with the Betatron Core particularly referencing earlier work [19].

Recalling Equation 2.21, a beam with non-zero (and typically negative) chromaticity Q' can have its tune distance δQ controlled by momentum $\Delta p/p$. The longitudinal voltage from the betatron core provides the resonance driving effect (red arrow in Figure 2.12), accelerating particles into resonance. Particles then experience unstable betatron oscillation, jumping between separatrices, before encountering an electrostatic septum, where they receive an extraction kick.

Tune Sweep

Tune sweep operates somewhat as the opposite of Betatron Core: rather than controlling the beam's tune distance away from resonance (δQ), moving the beam into resonance, the reference transverse tune of the machine (Q_x) is moved through the stationary waiting beam. This is illustrated, with a Stienbach diagram, in Figure 2.14.

For a small momentum spread $\Delta p/p$, the tune's dependency on quadrupole strength can be assumed as linear, so a simple quadrupole strength sweep is all that is required for tune-sweep.

There are, however disadvantages to this approach. Changing the quadrupole strength requires changing the optics of the machine, effectively creating a spread of magnetic rigidity ($B\rho$, Equation 2.10) in the beam. The effect of this is illustrated in Figure 2.15: particles excited into instability with different amplitudes will “lock on” to separatrices at different phase-space locations. The result is a range in angle of particles extracted at the electrostatic septum (located at, for example $x = 0.3$ in Figure 2.15).

Recalling Equation 2.71, amplitude A is correlated with momentum difference $\Delta p/p$. Given a real dispersion value (Equation 2.26), a condition can be computed which would align all separatrices on the septum:

$$D_n \cos(\pi - \Delta\phi) + D'_n \sin(\pi - \Delta\phi) = -\frac{4\pi}{3} Q'_x \quad \text{Eq. 2.72}$$

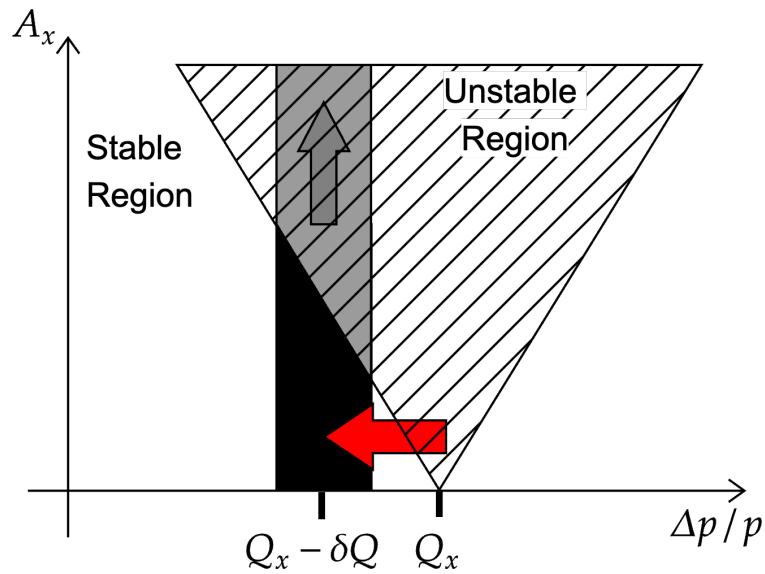


Figure 2.14: Stienbach diagram of tune-sweep slow extraction. Waiting beam in black, tune sweep effect in red, unstable beam in grey.

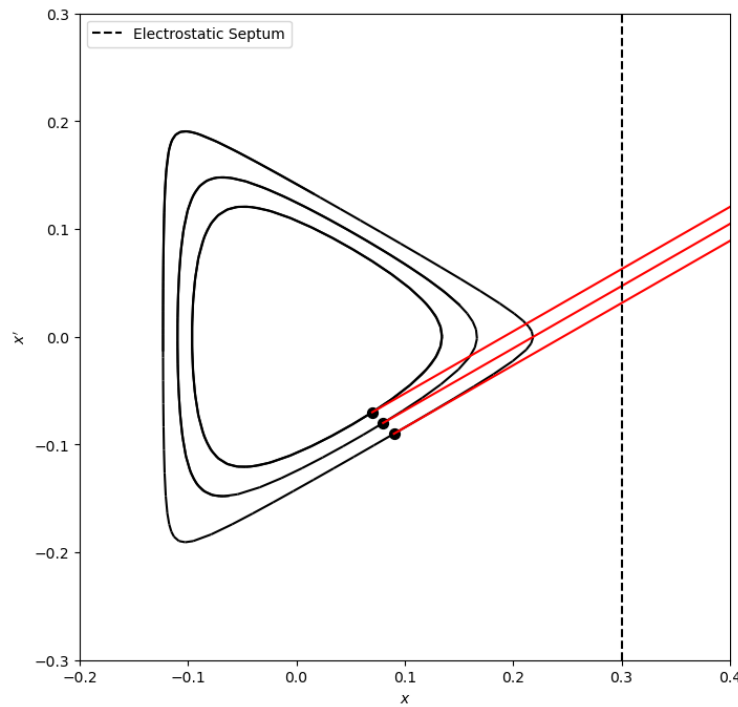


Figure 2.15: Phase-space map of three initial particles on the Kobayashi Hamiltonian, and one of their separatrices. An example electrostatic septum location is shown (dashed line).

This condition, known as the Hardt condition [20], will align the separatrices, given a phase advance $\Delta\phi$ and dispersion coefficients D_n, D'_n . However, in the context of tune-sweep extraction, the Hardt condition proves ineffective: a changing momentum will change dispersion coefficients, causing the separatrices to misalign.

COSE

To combat the effect of misaligned separatrices and differences in optics, *Constant-Optics Slow Extraction* (COSE) employs techniques of both betatron core and tune-sweep: the magnetic rigidity $B\rho$ (or reference momentum) of the beam is increased simultaneously with the tune-sweep.

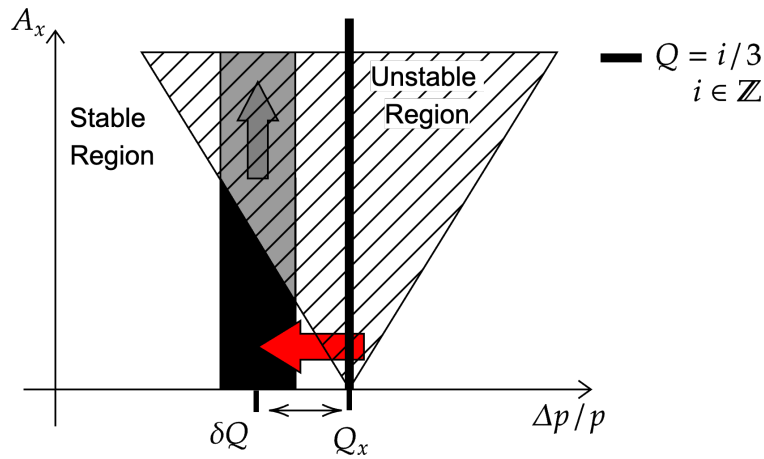


Figure 2.16: Stienbach diagram of COSE slow extraction. Waiting beam in black, tune sweep and optics ramp effect in red, unstable beam in grey.

This extraction method can be considered as betatron core extraction in the p_0 (reference momentum) frame of reference, rather than the p (particle momentum) frame of reference. By reformulating Equation 2.21 using p_0 , the following equation for tune distance δQ is obtained:

$$\delta Q = Q'_x \frac{p - p_0}{p_0} \quad \text{Eq. 2.73}$$

In this equation, betatron core slow extraction reduced δQ towards zero by changing p ; COSE does this by instead varying p_0 .

The exact process of COSE, and the other methods previously mentioned, varies between implementations. However, all of these methods are momentum-driven extraction, sharing the same principles and similar drawbacks. The most notable of these is high sensitivity to slight variations in machine optics (magnetic strengths). Small power supply ripples can have significant impacts to the “spill quality” obtained from these techniques. A betatron core with large inductance can reduce the effect of ripples by “smoothing out” current variations, but has the consequence of reducing the response rate, reducing the precision and controllability.

Another potential drawback arises when the beam is de-bunched during extraction so that the momentum of particles does not change [21]. If the extraction process is not complete and some particles remain in the waiting beam, they may have to be re-bunched and re-accelerated in order to be extracted, a process prone to inefficiency and losses.

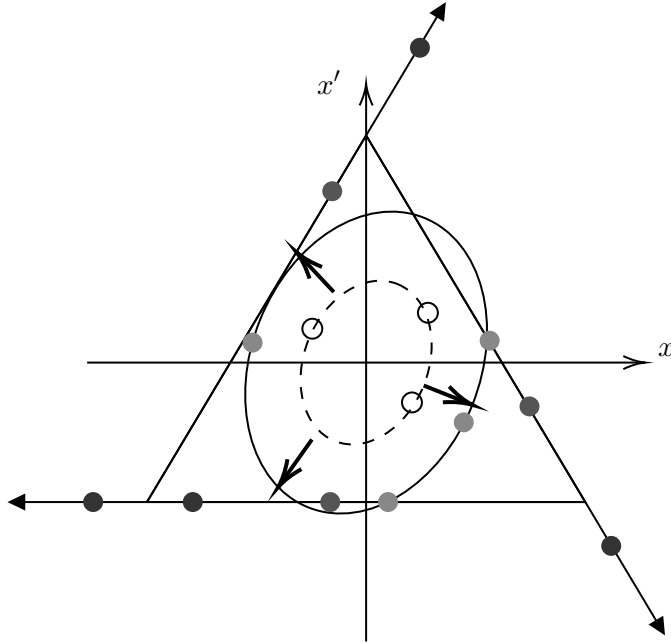


Figure 2.17: A phase-space schematic of RFKO, showing the emittance growth (dashed to solid ellipse) increasing the amplitude of a stable particle (white) into the unstable region (grey), where it moves along the separatrices (arrows) into extraction.

Radio-Frequency Knock-Out

Unlike the previously mentioned slow-extraction methods, Radio-Frequency Knock-Out (RFKO) is an amplitude- and sextupole-driven method. The principle of RFKO, as illustrated in Figure 2.17, is to excite particles into the resonant instability region by providing transverse “heating” of the beam—using a radio-frequency exciter to provide a small transverse kick to the beam, increasing its amplitude. This kick is provided at a third-integer fraction of the betatron tune, but a range of excitation frequency (frequency modulation, FM) is required as there is a range of momentum in the beam, and thus a range of tunes.

This method has been chosen for many East Area extraction implementations for a number of reasons. First, it allows for extraction while the beam is either bunched (longitudinally distributed in pulses, required for RF acceleration) or unbunched (with no longitudinal structure). A bunched extraction process allows for beam remaining in the machine after extraction to be re-accelerated and extracted, without the losses associated with re-bunching.

RFKO can also be used with an amplitude modulated (AM) excitation, which can be calibrated to provide a constant particle flux over time. However, for the experimental application in this thesis, AM was not used, as the extraction process took place over a long enough time period where flux was not a concern.

A variety of different signals can be used to drive the excitation: theoretically, white noise (a random signal with equal intensity at all frequencies) would be the ideal signal, providing a purely diffusive effect in phase space.

Chapter 3

Implementation and Simulation

3.1 RFKO Slow Extraction at the CERN PS

For implementation at the PS, and for use in extraction to East Area, a basic beam is set-up and configured for the East area. A proton beam momentum of 5.392 GeV/c was chosen for this study, as its magnetic rigidity is equivalent to the 750 MeV/c/nucleon Lead (Pb^{+54}) ions used for the CHIMERA experiment, with whom studies were carried out alongside, and it equates to a low enough energy as to not damage components during testing. This proton equivalent momentum is calculated as

$$B\rho = \frac{p}{q} = \frac{\sqrt{\left(\frac{E \cdot A}{E_0} + 1\right)^2 - 1}}{q} \quad \text{Eq. 3.1}$$

where A is the atomic mass, E is the proton energy per nucleon (0.75 GeV), and E_0 is the equivalent proton rest energy as calculated by

$$E_0 = Zm_p + Nm_n - \delta M \quad \text{Eq. 3.2}$$

where Z and N are the proton and neutron numbers, m_p and m_n are the proton and neutron rest masses, and δM is the mass defect of the nucleus.

Likewise, a single-bunch, low intensity beam (30×10^{10} particles/bunch) was chosen. The cycle was configured to use two standard beam-cycle periods of 1.2 s, in order to extend the window available for a spill to 500 ms.

3.1.1 Closed Orbit and Extraction Trajectory

As shown in Figure 3.1, the closed orbit of the PS differs at extraction than to that in normal operation. Four *bump* magnets, (BSW) create a large horizontal displacement at the two septa SMH57 and SMH61. This brings the closed orbit within range of the septum blades, where resonant particles can then cross the blade and enter the septum window.

The electrostatic septum, placed before the magnetic septa, is not used in this study, as it is skipped by the beam during ion extraction. It was decided that a proton implementation closer to the ion configuration would be advantageous, so that results can be compared to work carried out by CHIMERA.

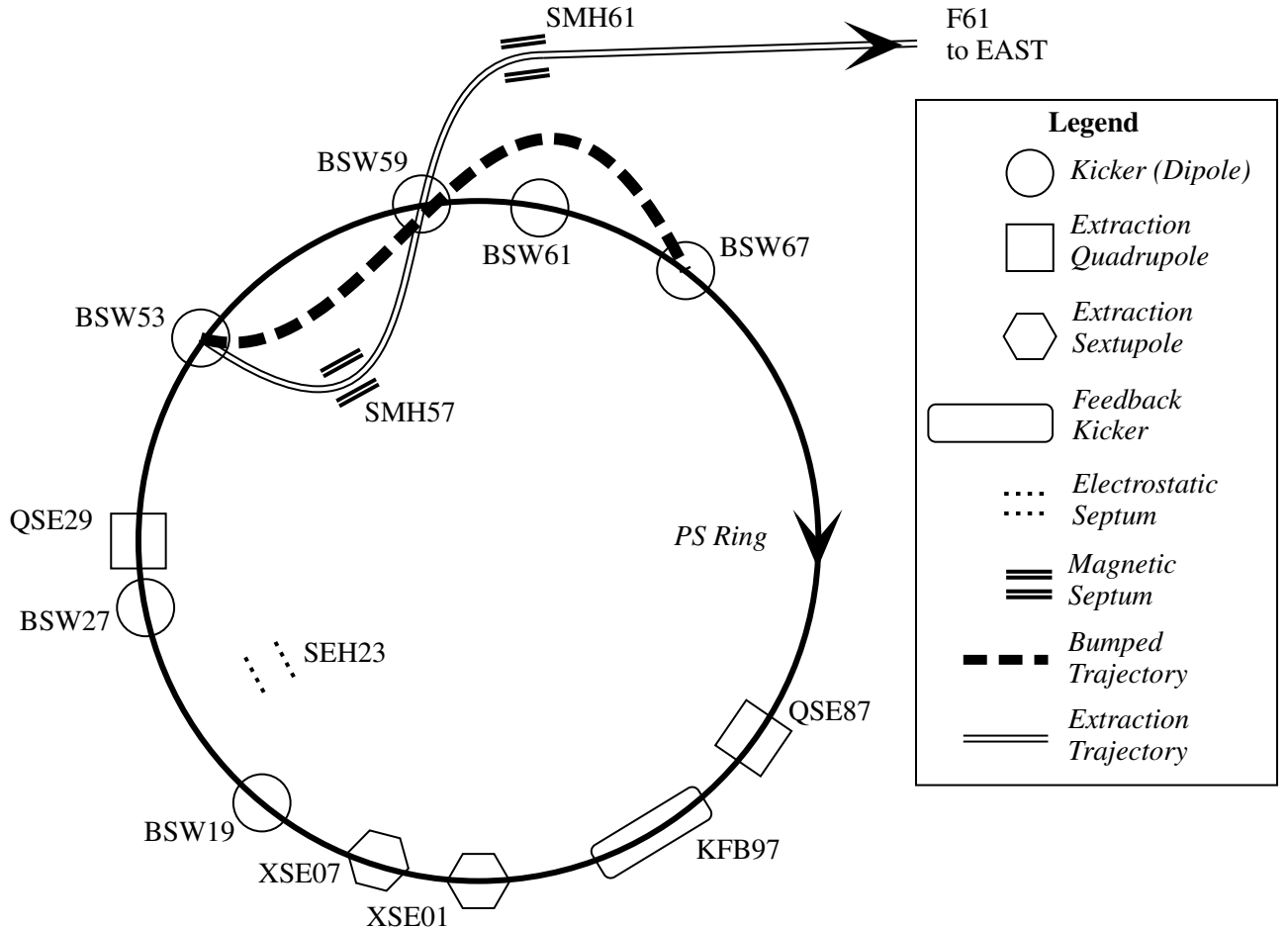


Figure 3.1: A schematic of the PS East extraction system, as configured for RFKO slow extraction. All important beamline elements are labelled with their CERN layout code. Also shown is the nominal orbit trajectory (solid line), the bumped trajectory (dashed line) created by the kicker magnets, and the extracted trajectory (double line) created by the magnetic septa.

3.1.2 Magnetic Cycle

The dipole magnetic field required for a $5.392 \text{ GeV}/c$ proton beam is calculated by

$$B = \frac{\frac{1}{c} \times 10^9 \cdot p}{\rho \cdot q} \quad \text{Eq. 3.3}$$

where the numerator converts the proton momentum from $\text{GeV} c_0^{-1}$ to T m . This is calculated as a field of 0.257 T.

In order to create the third-order resonance, the extraction sextupole system was enabled. This consists of a high-level parameter `PR.XSE/K`, which controls the sextupole normalised strength k_2 of the two extraction sextupoles, XSE01 and XSE07 (Figure 3.1).

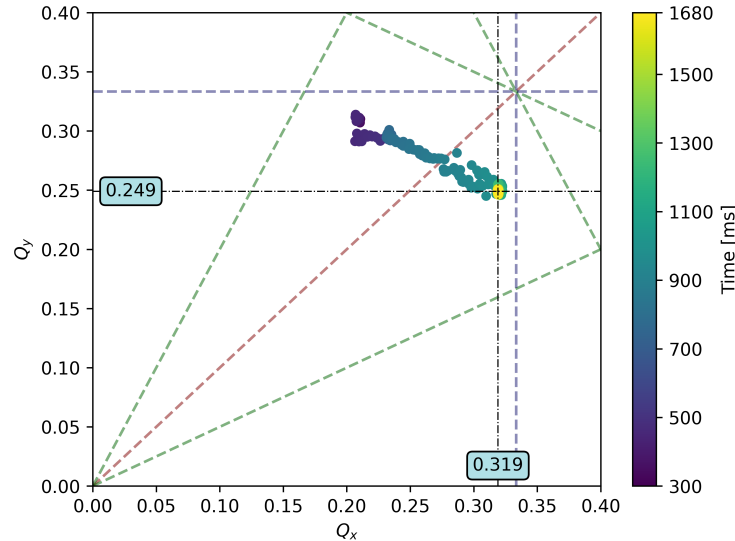


Figure 3.2: A tune map, plotting horizontal tune Q_x against vertical tune Q_y . Dashed lines indicate first order (red), second order (green) and third order (blue) resonances.

A high-level parameter QSE is also provided, which controls the normalised strength k_1 for a set of extraction quadrupoles (Figure 3.1). These serve to aid in betatron tune Q_x control, and to increase the amplitude β_x while decreasing the dispersion D_x at the septa locations. This large β_x allows the septum to be placed further from the circulating beam, and the small dispersion D_x satisfies the Hardt condition (Equation 2.72). These two parameters QSE and XSE, have been pre-configured for nominal East Area slow extraction, and are presented in Table 3.1.

Also present in this table are values for the high-level tune control knobs. These use the Pole Face Winding (PFW) magnets present in ever PS Main Unit dipole to control the horizontal and vertical betatron tune $Q_{x,y}$ and chromaticity $Q'_{x,y}$. Tune control was very important to the set-up of this implementation—the horizontal tune was positioned close to the third-order resonance, at 0.32. The chromaticity (tune spread) was minimised to avoid fractions of the waiting beam being at resonance before the RFKO was activated, which would cause a low-level initial uncontrolled spill. Meanwhile, the vertical tune was kept away from any resonances. This tune control is shown in Figure 3.2, which plots hoizontal tune against vertical tune. This provides an easy understanding of first, second, and third order resonances caused by coupling between the two planes. This coupling resonance is avoided by the following condition:

$$m \cdot Q_x + n \cdot Q_y \neq p \quad \text{Eq. 3.4}$$

where m , n , and p are arbitrary integers. Also used is the fractional tune split, Δ , defined as

$$\Delta = Q_x - Q_y - p \quad \text{Eq. 3.5}$$

From Figure 3.3, we find the tune split at injection $\Delta = -0.1$, and at extraction $\Delta = 0.07$, both of which avoid coupling resonances.

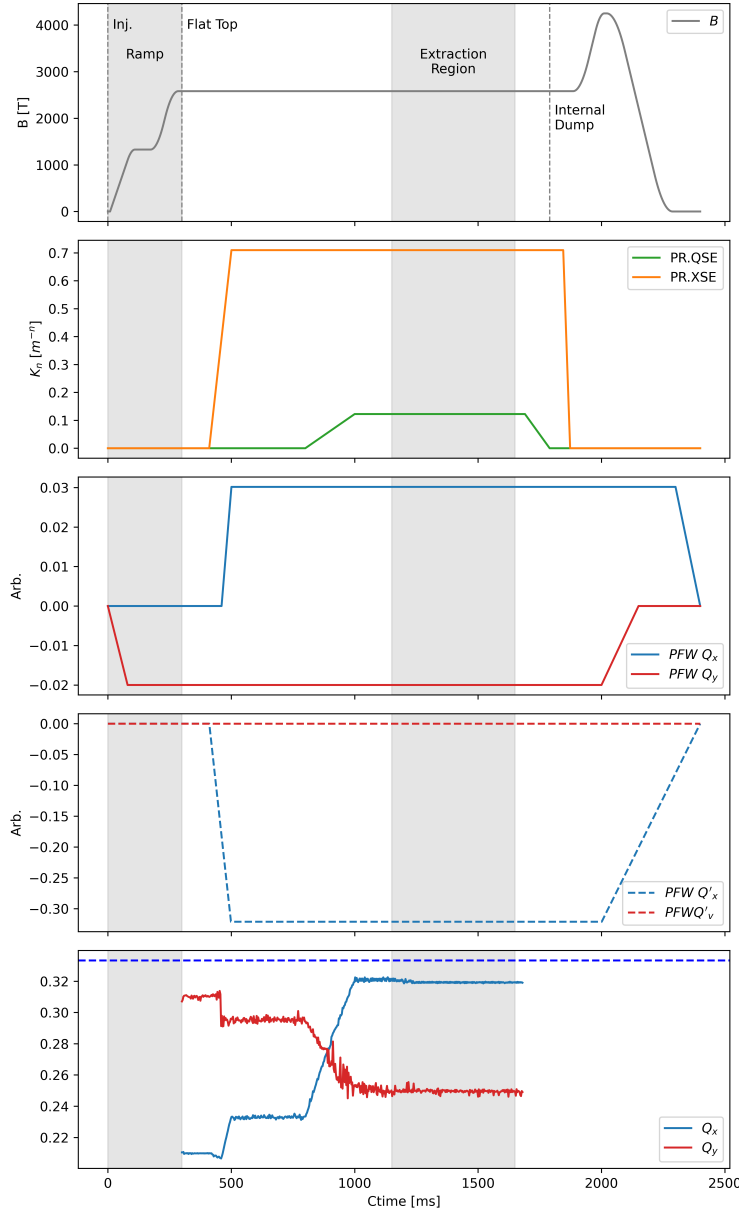


Figure 3.3: Graphs of the parameters presented in Table 3.1, showing the high-level parameter configuration for the implementation of East Area RFKO slow extraction. Top graph shows the bending dipole B field, points of injection (from PSB) and dumping (internal absorption of remaining beam), and regions of acceleration (ramp) and stable period for extraction. Second graph shows multipole components k_n for extraction quadrupole ($k = 1$) and sextupole ($k = 2$). Second and third graphs show tune control configuration with the pole face winding (PFW) magnets. Final graph shows fractional betatron tune measurements for horizontal and vertical plane.

Parameter	Value	Ramp Up Time	Ramp Down Time	Ramp Time Length
QSE	0.1225	800	1690	200
XSE	0.7097	410	1845	90
Q_x	0.0302	460	2300	40
Q'_x	-0.3211	410	2000	90
Q_y	-0.02	0	2200	80
Q'_y	0	n/a	n/a	n/a

Table 3.1: Table of configured high-level parameters for the implementation of East Area RFKO slow extraction.

Parameter	Value
Chirp Start [Hz]	$0.3 \cdot f_{rev}$
Chirp Stop [Hz]	$0.35 \cdot f_{rev}$
Chirp Repetition [ms]	1
Chirp Turns	256

Table 3.2: Initial parameters for RFKO extraction using the *Qmeter* control program.

3.1.3 Transverse Excitation

Once a basic, stable cycle is configured in the PS, the transverse excitation is implemented. This uses a transverse kicker located at section 97 of the PS, KFB97, a ~ 1 m long strip-line kicker, with both horizontal and vertical planes [22]. With a peak RF power of 5000 W across the two electrodes, and an impedance of 100Ω , the transverse feedback (TFB) kicker can provide a peak voltage at 1000 V and current of 10 A. The electric and magnetic fields are then, defined as

$$\vec{E} = \frac{V}{r} \quad \text{Eq. 3.6}$$

$$\vec{B} = \frac{2I}{2\pi r} \cdot \mu_0 \quad \text{Eq. 3.7}$$

where r is the electrode aperture 70 mm. The electric and magnetic deflection angles are then [23, 3.1-3.2]

$$\theta_E = \frac{\vec{E}/1 \times 10^9 \cdot L}{pc/1 \times 10^9 \cdot \beta} \quad \text{Eq. 3.8}$$

$$\theta_B = \frac{c/1 \times 10^9 \cdot \vec{B} \cdot L}{pc/1 \times 10^9} \quad \text{Eq. 3.9}$$

where L is the electrode length 935 mm. The summation of these two angles provides a maximum deflection of 10.814 605 μ rad.

To drive this transverse kicker, two systems were used. Initially, the *Qmeter* control program [24] provided an interface to this kicker. While the program was designed—and used extensively in this study—for tune measurements, it can be exploited to provide a frequency-modulated *chirp* signal across the transverse kicker. The program was used to configure the *start* and *stop* frequencies for the frequency-modulated chirp (as unit interval multiples of the revolution frequency f_{rev}), chirp length (in 2^n revolutions), and the time after which the chirp would repeat (in milliseconds). This produced the effect of a frequency-modulated chirp windowed by a square signal (Figure 3.4). Previous studies [25] found suitable parameters to produce a baseline RFKO extraction implementation, tabulated in Table 3.2, and found a significant dependency of spill quality on the chirp repetition rate.

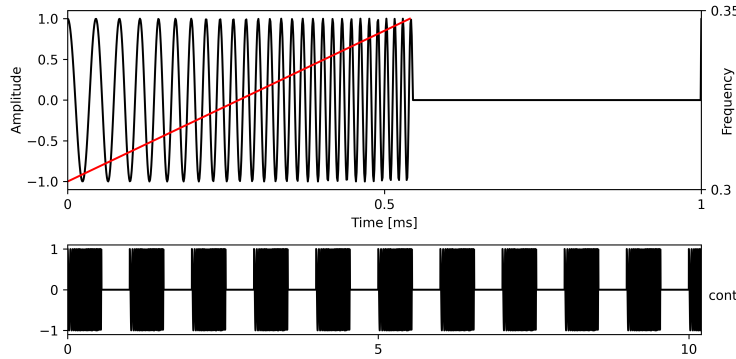


Figure 3.4: An example of the chirp signal generated by the *Qmeter* application; a frequency-modulated chirp windowed by a square signal.

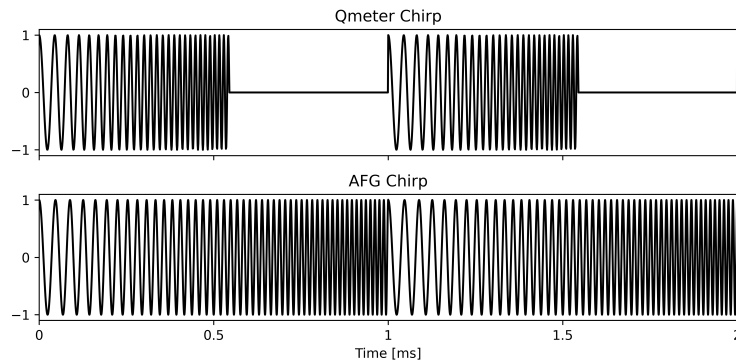


Figure 3.5: An example of the chirp signal generated by *Qmeter* (top) and by the arbitrary function generator (AFG) (bottom).

To explore chirp repetition rates above the 1 kHz (below 1 ms) limit of *Qmeter*, a new signal generator was configured to control the TFB kicker plates. This function generator was configured as a two-channel source, channel 1 being a sine wave with a frequency modulated by channel 2, a ramp/sawtooth wave. By choosing a central frequency and frequency deviation corresponding to the chirp generated by *Qmeter*, the function generator was able to produce a similar signal to that of the *Qmeter* system, but not windowed by a square function (Figure 3.5). This allowed for chirp repetition rates of 1 kHz and above, and was used to explore the effect of chirp repetition rate on spill quality.

3.2 RFKO Slow Extraction in Simulation

As motivated in section 1.1, the majority of work surrounding the results presented in this thesis was towards developing a simulation framework to accurately model the spill structure of RFKO at the PS. This section will detail the simulation tools used, the implementation of the RFKO extraction simulation, and the methods used to compare the simulation results to machine data.

3.2.1 Simulation Tools

A variety of simulation software packages for accelerator physics are available, each having their own optimisations, and application areas amongst the accelerator physics community. For this study, the MAD-X [8]

and Xsuite [26] packages were used. MAD-X remains the standard tool in the area of optics and beam transfer, and CERN provides a common optics repository—acc-models [27]—containing MAD-X *sequence* files which describe the optics lattices for the CERN accelerator complex. For the PS, many *scenarios* are provided alongside the operational models, one of which is a pre-configured for East Area slow extraction.

Xsuite—a relatively new simulation tool, being released in 2021—is a Python package which shares many similarities with MAD-X, and can import MAD-X sequences into its own lattice definitions. Xsuite provides many functions which build upon MAD-X’s capabilities, such as *context* management, which provides the ability to run simulations on different hardware—namely GPUs. This is achieved by using the cupy [28] package, which provides a drop-in replacement for numpy, but with optimisations for accelerating workloads on GPUs. Additionally, Xsuite also has a pre-defined Exciter beam element, which models the time-dependent transverse kicker used in RFKO. These two capabilities motivated its use in this study.

3.2.2 Lattice Configuration

The *East Area Extraction* scenario provided by acc-models was used as the basis for all simulation models, and was modified to include the parameters outlined in Table 3.1. This generated lattice file—defining the strengths and location for all 2664 beam elements—was used to produce the optics plots shown in Figure 3.6, which displays how the kicker magnets create large displacements at the extraction septa, and how dispersion is controlled by the extraction quadrupoles.

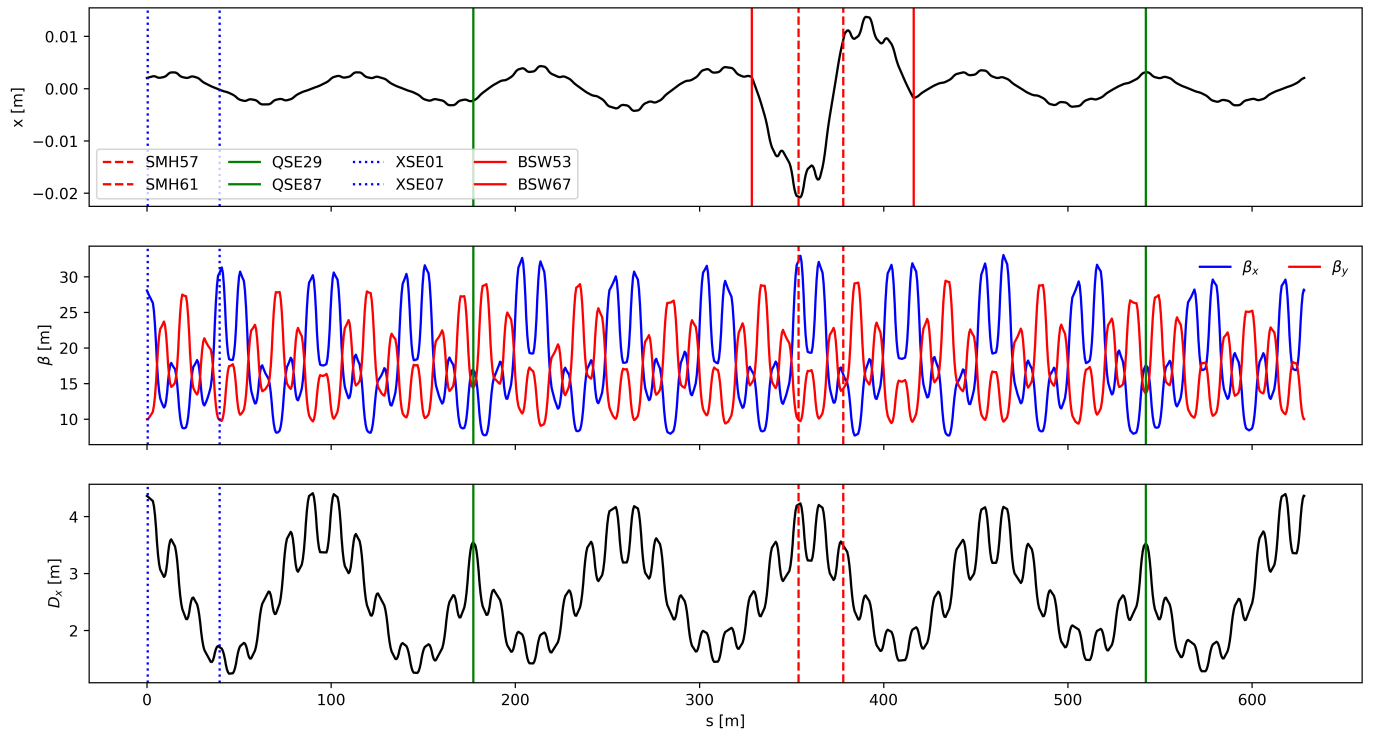


Figure 3.6: Optics plots of the stable particle for the acc-models PS East Area extraction scenario. Top figure shows transverse displacement x , middle figure shows twiss beta function β , and bottom figure shows transverse dispersion D_x . Also labelled are key extraction elements: the magnetic septa (SMH), the extraction quadrupoles (QSE), extraction sextupoles (XSE), and kickers (BSW)

This lattice was then imported to `Xsuite`, where the custom RFKO beam elements could be included. These elements were:

- An `Exciter`, modelling the TFB kicker KFB97.
- A `LimitRect`, modelling the magnetic septum SMH57.
- A `Cavity`, modelling the RF cavities providing acceleration and longitudinal focusing, operating at the 8th harmonic.

Exciter

Using Equation 3.8 and Equation 3.9, a function (Listing B.1) was written to convert the voltage applied across the TFB kicker to the angle of deflection generated by the electric and magnetic fields. This value was then used to define the strength of the `Exciter` element, which was placed at the location of the TFB kicker in the lattice. Another function (Listing B.2) was written to generate the chirp signal as generated by *Qmeter* and the arbitrary function generator (AFG). This function was then used to define the `Exciter` element's `samples` parameter, which is used to define the time-dependent kick.

Septum

The first magnetic septum, SMH57, was modelled as a simple rectangular aperture `LimitRect`. By setting this aperture to coordinates corresponding to the window of the septum, particles which are lost to the aperture can be considered as extracted. As this is the only aperture modelled, it can be assumed that particles lost to an aperture limit—with `Xsuite` particle state 0 (flag `XT_LOST_ON_APERTURE`)—entered the window of the septum.

RF Cavity

A single RF cavity was added to the model, corresponding to the RF system of the PS. While the real system comprises of many such cavities, modelling a single cavity with the total RF voltage applied provides an accurate representation of the longitudinal dynamics of the beam, given there are no other longitudinal elements present in the model.

3.2.3 Distribution Generation

To accurately simulate the conditions used in the RFKO studies, the initial particle distribution must be generated using machine measurements. The parameters used included:

- Beam momentum p [GeV c_0^{-1}]
- Intensity I [proton/bunch]
- Horizontal RMS emittance ε_x
- Longitudinal RMS emittance ε_x [eV s]

These values were obtained during machine studies. The beam momentum and intensity were controlled values, configured by high-level machine parameters. The horizontal emittance ε_x was measured using Secondary Emission Monitor (SEM) grids [29], and the vertical emittance ε_z using tomography of the Beam Current Transformer (BCT) profile [30]. The measured values are shown in Table 3.3. The beam distribution

Parameter	Value
Beam Momentum p [GeV/c]	5.392
Intensity N [proton/bunch]	3×10^{11}
Horizontal Emittance ε_x [mm mrad]	2.38
RMS Longitudinal Emittance [eVs]	0.276

Table 3.3: Initial parameters particle generation, corresponding to measurements made during machine studies.

was then generated according to these parameters, “matched” to the model longitudinal dynamics of the model by Xsuite.

It was decided that the simulation code will generate a new distribution each time it was initiated. With a sufficiently large number of particles, these random distributions will be statistically similar. This prevented the need to transfer a large, persistent file to each simulation job; this transfer time was, qualitatively, found to be longer than the time taken to generate a new distribution file of the same size.

3.2.4 Simulation Process

Once an initial simulation process was built, one issue became immediately apparent: to simulate the full 0.5 s extraction region (Figure 3.3), the simulation needed to process approximately 235,000 turns. To produce a statistically significant extraction rate, the a sufficient number of particles—roughly 500,000—needed to be generated and simulated. A typical desktop computer, for instance, would require over 600 hours to complete such a simulation, at a rate of roughly 13 s/iteration.

To accelerate the simulation speed to a more reasonable rate, two tools were employed. While not unique to Xsuite, they are both simplified by the package. The first method was the simplest: as mentioned previously, Xsuite provides ready-to-go compatibility with CuPy and CUDA GPU acceleration. The second method relies on CERN’s Batch Service, a high-throughput computing service which allows users to submit jobs via the *HTCondor* framework.

To submit the simulation jobs to the batch processing service, the simulation software was *containerised* using a Docker [31] image. This image provides a complete environment for the simulation, including a distribution of Python, the Xsuite package, the CuPy package, and various other dependencies. This image was made available on CERN’s image registry, where it could be used by the batch service for each simulation. This container [32] eliminated the need to set up the simulation environment on each machine, and ensures that the simulation is run in a consistent environment, and enabled the use of HTCondor’s GPU resources.

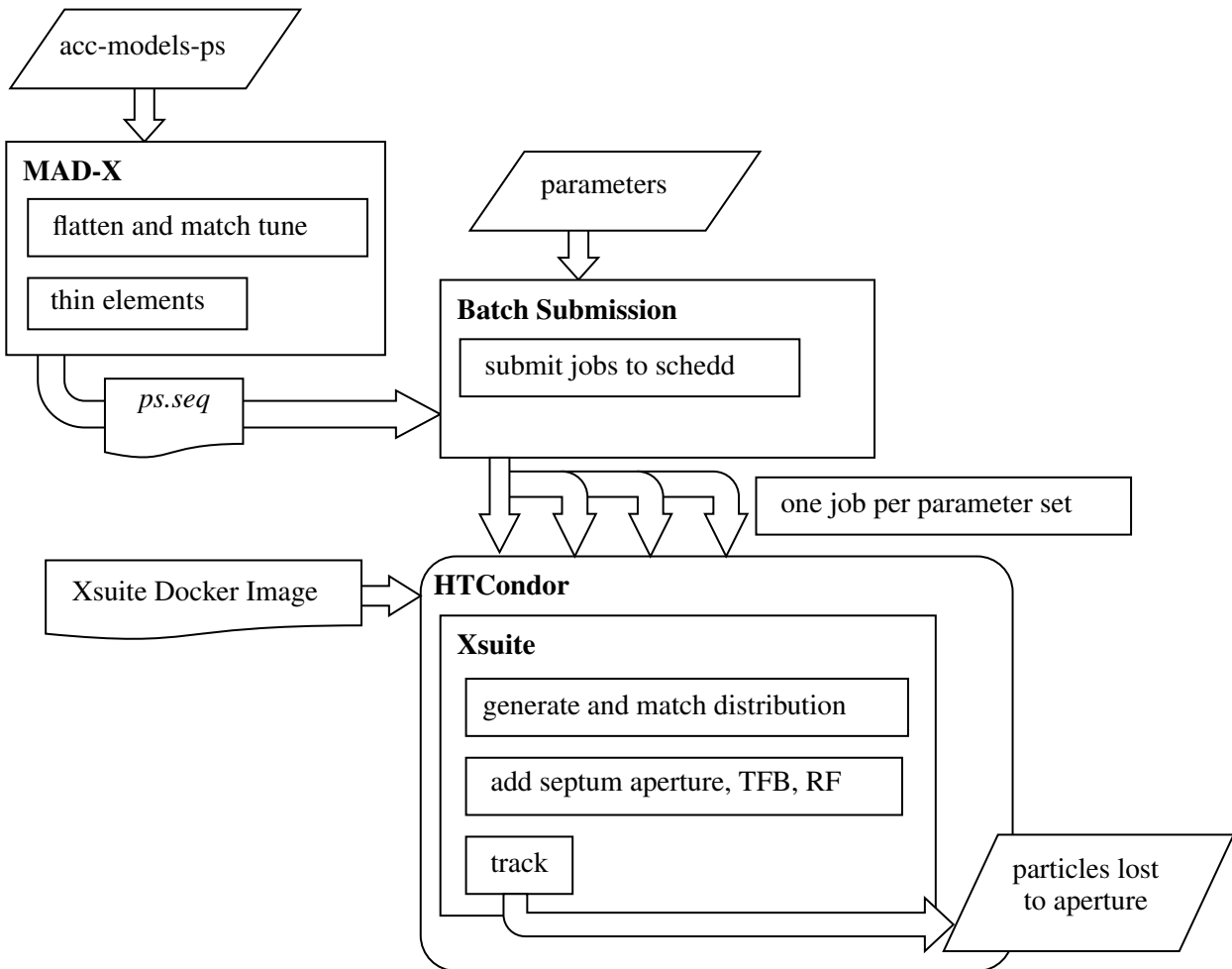


Figure 3.7: A flowchart describing an overview of the simulation process

Chapter 4

Analysis

Xsuite was successfully used to simulate RFKO slow extraction at the PS. This section presents the results of this simulation, comparing both

- the computation time between different platforms, and
- the results of the simulation with the results of the real machine.

4.1 Computation Time

Previous work [33] on optimising simulations slow extraction (at the SPS) achieved a simulation time of 7 hours 30 minutes (27 000 s) for a total of 200 000 turns and 1000 particles, using a similar batching process, but without the advantage of GPU acceleration. The simulation process described in subsection 3.2.4 achieved a total time of

4.2 Frequency Response

In order to compare the accuracy of RFKO simulations to the implementation on the real machine, analytical tools established by previous work [34] were used to measure the frequency response of the RFKO system. By varying the rate at which a chirp was repeated, known as the *interval frequency* or *rep rate*, the resulting spill could be characterised.

For the real machine implementation, the spill was measured using N2 gas scintillators [35] located in the F61 extraction line (see Figure 3.1). These scintillators are measured by various devices: the interface BXSCAL was selected, which provided time-series measurements of particle counts at ~ 18.8 kHz. The spill was measured for a range of interval frequencies.

The same was performed for simulations; the turn number at which a particle was lost to the aperture was recorded, along with its longitudinal ζ variable, defined as

$$\zeta = s \frac{\beta}{\beta_0} - \beta c t \quad \text{Eq. 4.1}$$

where β is the relativistic lorentz factor. This was used to reconstruct the exact time at which the particle was lost to the aperture—and thus considered as extracted—using an equation used by the Exciter beam

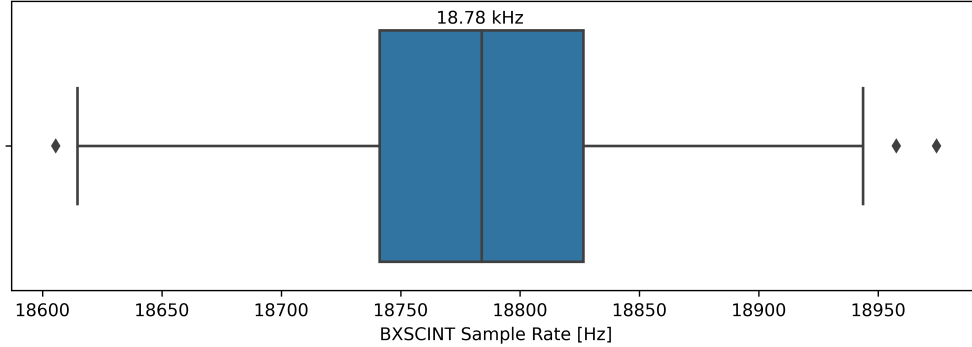


Figure 4.1: Variation in sample rate of the BXSCAL device over the course of the measurement.

element:

$$t = Nt_{rev} - \frac{\zeta}{\beta_0 c} \quad \text{Eq. 4.2}$$

where $t_{rev} = 1/f_{rev}$, the machine revolution time, and N is the turn at which the particle was lost. This time-series data was then re-binned down to the same frequency of the real machine measurement.

The time-series spill signal was then analysed using a discrete Fourier transform (DFT) to obtain the frequency response of the system. Using a peak-finding algorithm to allow for slight variation in spill measurement frequency—over the measurements used, the BXSCAL sample rate varied between 18.6 kHz and 18.95 kHz (Figure 4.1). As this variation was evenly distributed around the mean value of 18.78 kHz, the DFT was largely unaffected.

Once the DFT was computed, the interval rate for each measurement was selected, normalised by the DFT DC component (the 0 Hz term, equivalent to the average of all samples), and the magnitude of the resulting complex number was plotted against the interval frequency. This analysis was performed for both the real machine and the simulations, with both a bunched beam (with RF cavities enabled) and a coasting/debunched beam (with RF cavities disabled). The results are shown in Figure 4.2 and Figure 4.3 for the bunched and coasting beams respectively.

A low-pass filter effect, which was anticipated by previous studies [36], is clearly visible in both Figure 4.2 and Figure 4.3.

4.3 Spill Duty Factor

$$\tau = \frac{\langle x \rangle^2}{\langle x^2 \rangle} \quad \text{Eq. 4.3}$$

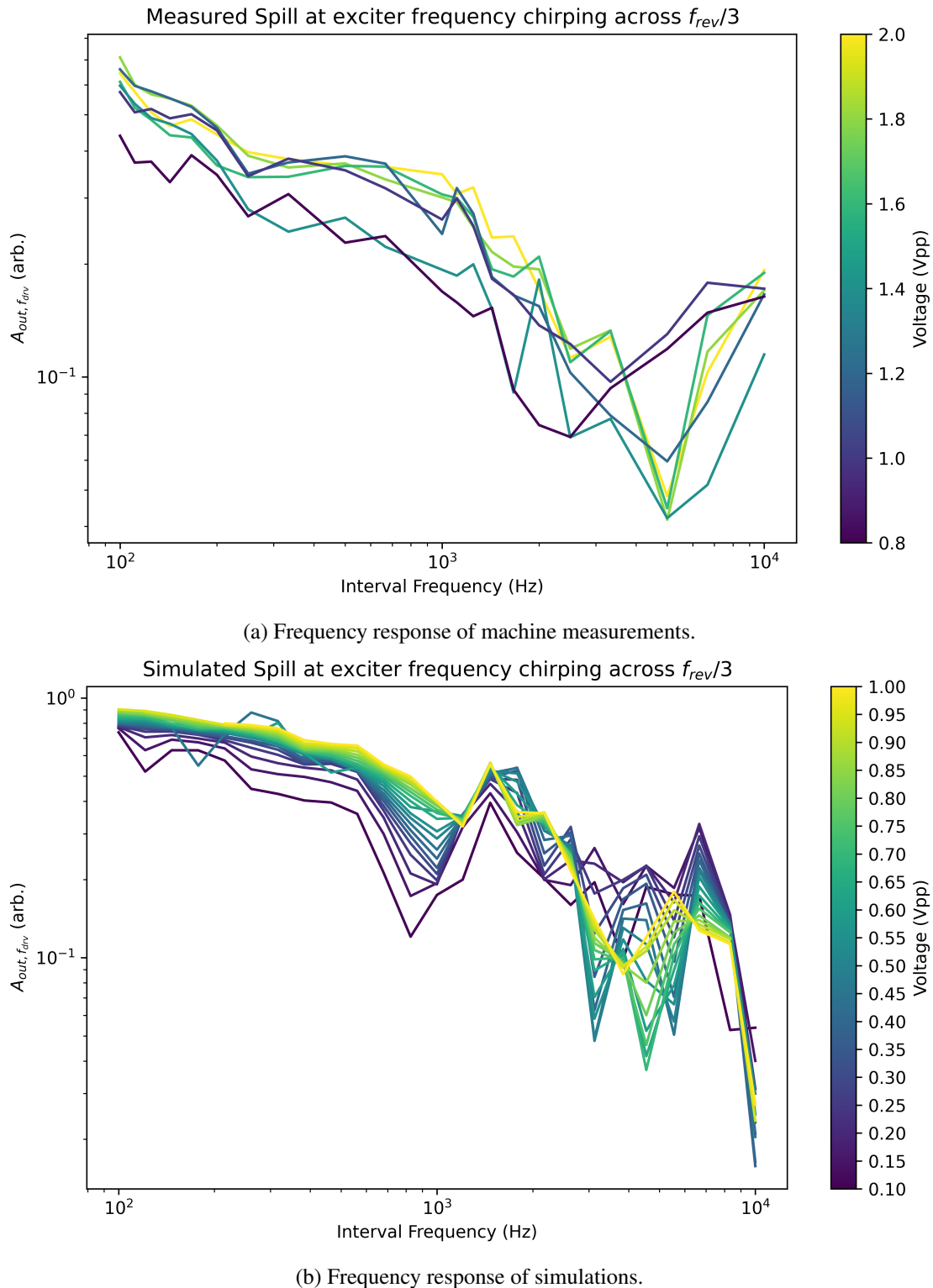
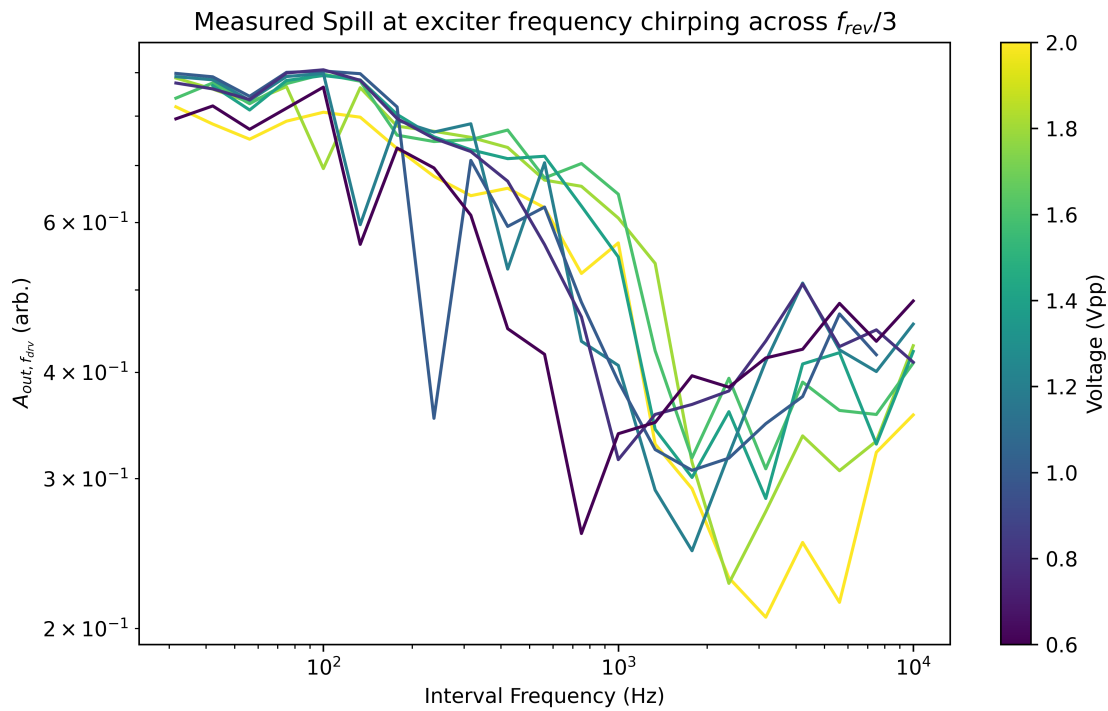


Figure 4.2: Frequency response of the RFKO system, **with RF cavities enabled**, both in the real machine and in simulation.



(a) Frequency response of machine measurements.



(b) Frequency response of simulations.

Figure 4.3: Frequency response of the RFKO system, **with RF cavities disabled**, both in the real machine and in simulation.

Chapter 5

Conclusion

Chapter 6

Acknowledgements

Bibliography

- [1] M. Fraser, P. A. Arrutia Sota, K. Biłko, N. Charitonidis, S. Danzeca, M. Delrieux, M. Duraffourg, N. Emriskova, L. S. Esposito, R. García Alía, A. Guerrero, O. Hans, G. Imesch, E. Johnson, G. Lerner, I. Ortega Ruiz, G. Pezzullo, D. Prelipcean, F. Ravotti, F. Roncarolo, and A. Waets, “Feasibility of Slow-Extracted High-Energy Ions From the CERN Proton Synchrotron for CHARM,” *JACoW IPAC*, vol. 2022, pp. 1703–1706, 2022. [Online]. Available: <https://cds.cern.ch/record/2845894>
- [2] M. A. Fraser, “Fast extraction: single and multi-turn,” vol. Vol 5. CERN, 2018, p. Extraction and Transfer. [Online]. Available: <https://doi.org/10.23730/CYRSP-2018-005.285>
- [3] K. D. Metzmacher and L. Sermeus, “The PSB Ejection and Recombination Kicker Systems for LHC,” CERN, Geneva, Tech. Rep., 2000. [Online]. Available: <http://cds.cern.ch/record/2061508>
- [4] S. Ghithan, G. Roy, and S. Schuh, “Design study of beam transport lines for BioLEIR facility at CERN,” *JINST*, vol. 12, no. 09, p. P09019, 2017.
- [5] K. J. le Couteur, “The regenerative deflector for synchro-cyclotrons,” *Proceedings of the Physical Society. Section B*, vol. 64, no. 12, p. 1073, dec 1951. [Online]. Available: <https://dx.doi.org/10.1088/0370-1301/64/12/308>
- [6] K. J. L. Couteur, “The extraction of the beam from the liverpool synchrocyclotron.” *Proceedings of the Royal Society of London. Series A, Mathematical and Physical Sciences*, vol. 232, no. 1189, pp. 236–241, 1955. [Online]. Available: <http://www.jstor.org/stable/99763>
- [7] P. A. Arrutia Sota, P. Burrows, A. De Franco, M. Fraser, B. Goddard, V. Kain, F. Kuehneubl, M. Pivi, D. Prokopovich, and F. Velotti, “Implementation of a Tune Sweep Slow Extraction with Constant Optics at MedAustron,” *JACoW IPAC*, vol. 2022, pp. 1715–1717, 2022. [Online]. Available: <https://cds.cern.ch/record/2845862>
- [8] F. C. Iselin, “The MAD Program (Methodical Accelerator Design): Reference Manual,” 5 1985. [Online]. Available: <https://inspirehep.net/literature/214504>
- [9] H. Wiedemann, *Introduction to Accelerator Physics*. Cham: Springer International Publishing, 2015, pp. 3–41. [Online]. Available: https://doi.org/10.1007/978-3-319-18317-6_1
- [10] L. Nevay, J. Snuverink, A. Abramov, L. Deacon, H. Garcia-Morales, H. Lefebvre, S. Gibson, R. Kwee-Hinzmann, W. Shields, S. Walker, and S. Boogert, “Bdsim: An accelerator tracking code with particle-matter interactions,” *Computer Physics Communications*, vol. 252, p. 107200, 02 2020.
- [11] J. Rossbach and P. Schmüser, “Basic course on accelerator optics,” 1994. [Online]. Available: <http://cds.cern.ch/record/247501>

- [12] E. Courant and H. Snyder, “Theory of the alternating-gradient synchrotron,” *Annals of Physics*, vol. 3, no. 1, pp. 1–48, 1958. [Online]. Available: <https://www.sciencedirect.com/science/article/pii/0003491658900125>
- [13] R. D. Ruth, “An Introduction to Particle Accelerators,” *Physics Today*, vol. 55, no. 8, pp. 52–52, 08 2002. [Online]. Available: <https://doi.org/10.1063/1.1510283>
- [14] F. Tecker, “Longitudinal Beam Dynamics in Circular Accelerators,” in *CAS - CERN Accelerator School 2019: Introduction to Accelerator Physics*, 11 2020.
- [15] Y. Kobayashi, “Theory of the resonant beam ejection from synchrotrons,” *Nuclear Instruments and Methods*, vol. 83, no. 1, pp. 77–87, 1970. [Online]. Available: <https://www.sciencedirect.com/science/article/pii/0029554X70905379>
- [16] L. Falbo, E. Bressi, S. Foglio, and C. Priano, “Betatron Core Slow Extraction at CNAO,” in *Proc. 9th International Particle Accelerator Conference (IPAC’18), Vancouver, BC, Canada, April 29-May 4, 2018*, ser. International Particle Accelerator Conference, no. 9. Geneva, Switzerland: JACoW Publishing, June 2018, paper TUZGBF3, pp. 1237–1239, <https://doi.org/10.18429/JACoW-IPAC2018-TUZGBF3>. [Online]. Available: <http://jacow.org/ipac2018/papers/tuzgbf3.pdf>
- [17] P. A. Arrutia Sota and M. A. Fraser, “Optimisation of Slow Extraction and Beam Delivery from Synchrotrons,” 2020, presented 2020. [Online]. Available: <https://cds.cern.ch/record/2749240>
- [18] L. Badano, M. Benedikt, P. J. Bryant, M. Crescenti, P. Holy, A. T. Maier, M. Pullia, S. Rossi, and P. Knaus, *Proton-Ion Medical Machine Study (PIMMS)*, 1, 2000. [Online]. Available: <https://cds.cern.ch/record/385378>
- [19] L. Badano and S. Rossi, “Characteristics of a betatron core for extraction in a proton-ion medical synchrotron,” CERN, Geneva, Tech. Rep., 1997. [Online]. Available: <http://cds.cern.ch/record/327305>
- [20] M. Pullia, “Hardt condition for superposition of separatrices,” *Informal Meeting on Slow Extraction from Synchrotrons for Cancer Therapy*, 1996. [Online]. Available: <https://cds.cern.ch/record/1425424>
- [21] K. A. Brown, “Third integer resonant extraction: Ripple compensation and bunched beams,” 7 2021. [Online]. Available: <https://www.osti.gov/biblio/1805240>
- [22] G. Sterbini, A. Blas, and S. Gilardoni, “Beam-based Performance of the CERN PS Transverse Feedback,” p. MOPAB10, 2015. [Online]. Available: <https://cds.cern.ch/record/2158994>
- [23] C. Bovet, R. Gouiran, I. Gumowski, and K. H. Reich, *A selection of formulae and data useful for the design of A.G. synchrotrons; rev. version.* Geneva: CERN, 1970. [Online]. Available: <https://cds.cern.ch/record/104153>
- [24] M. Gasior and R. Jones, “High Sensitivity Tune Measurement by Direct Diode Detection,” 2005. [Online]. Available: <https://cds.cern.ch/record/895142>
- [25] T. Bass, “Benchmarking simulations of slow extraction driven by rf transverse excitation at the cern proton synchrotron,” in *Proc. IPAC’23*, ser. IPAC’23 - 14th International Particle Accelerator Conference, no. 14. JACoW Publishing, Geneva, Switzerland, 05 2023, paper TUPM116, pp. 2458–2461. [Online]. Available: <https://indico.jacow.org/event/41/contributions/1678>
- [26] “Xsuite.” [Online]. Available: <xsuite.web.cern.ch>
- [27] “Cern optics repository.” [Online]. Available: <https://acc-models.web.cern.ch/acc-models/>
- [28] R. Okuta, Y. Unno, D. Nishino, S. Hido, and C. Loomis, “Cupy: A numpy-compatible library for nvidia gpu calculations,” in *Proceedings of Workshop on Machine Learning Systems (LearningSys) in The*

- Thirty-first Annual Conference on Neural Information Processing Systems (NIPS)*, 2017. [Online]. Available: http://learningsys.org/nips17/assets/papers/paper_16.pdf
- [29] M. Martini and H. O. Schönauer, “Emittance measurements in the CERN PS complex,” *Part. Accel.*, vol. 58, pp. 137–151, 1997. [Online]. Available: <https://cds.cern.ch/record/324553>
- [30] S. Hancock and S. A. J-L, “A pedestrian guide to online phase space tomography in the CERN complex,” CERN, Geneva, Tech. Rep., 2001. [Online]. Available: <http://cds.cern.ch/record/960231>
- [31] D. Merkel, “Docker: lightweight linux containers for consistent development and deployment,” *Linux journal*, vol. 2014, no. 239, p. 2, 2014.
- [32] “Xsuite-batch docker image.” [Online]. Available: <https://gitlab.cern.ch/tbass/xsuite-docker>
- [33] P. Schicho, “Optimizing Simulation Times of SPS Slow Extraction using MAD-X,” 2015. [Online]. Available: <http://cds.cern.ch/record/2039579>
- [34] M. Pari, F. M. Velotti, M. A. Fraser, V. Kain, and O. Michels, “Characterization of the slow extraction frequency response,” *Phys. Rev. Accel. Beams*, vol. 24, no. 8, p. 083501, 2021. [Online]. Available: <https://cds.cern.ch/record/2780495>
- [35] P. Actis, T. Dorenbos, and C. Johnson, “An optically coupled differential beam time structure monitor for slow extraction,” CERN, Geneva, Tech. Rep., 1976. [Online]. Available: <https://cds.cern.ch/record/2831368>
- [36] K. Okamura, Y. Arakaki, T. Kimura, S. Murasugi, R. Muto, Y. Shirakabe, M. Tomizawa, and E. Yanaoka, “A consideration on the transfer function between rq field and slow extraction spill in the main ring of j-parc,” *Proceedings of the 10th Int. Particle Accelerator Conf.*, vol. IPAC2019, p. Australia, 2019. [Online]. Available: <http://jacow.org/ipac2019/doi/JACoW-IPAC2019-WEPMP008.html>

Appendix A

Derivations

A.1 Relating longitudinal variables

In order to relate the dispersive and chromatic functions produced by MAD-X to those calculated by Xtrack, we must multiply MAD-X's results by the relativistic Lorentz factor $\beta = v/c$. This is because MAD-X uses the relative momentum error δ_p as a longitudinal variable, defined as

$$\delta_p = \frac{p - p_0}{p_0} \quad \text{Eq. A.1}$$

, where p is the momentum of the particle, and p_0 the momentum of the *reference* (or *design*) particle, whereas Xtrack uses the relative energy error

Appendix B

Code Snippets

```

1 from scipy.constants import physical_constants as const
2 import numpy as np
3
4 p = 5.392 # GeV/c, proton momentum for the cycle
5 Brho = p*3.3356 # Tm, magnetic rigidity
6
7 def kick_angle(voltage):
8     """
9         Calculates the angular kick to a proton beam of rigidity 'Brho' [Tm] from a
10        pair of TFB electrodes with voltage 'voltage' [V].
11    """
12
13    c = const["speed of light in vacuum"] # [m/s] speed of light
14    E0 = const["proton mass energy equivalent in MeV"][0]*1e6 # eV
15    mu0 = const["vacuum mag. permeability"][0] # H/m, vacuum permeability
16
17    T = (np.sqrt(Brho**2+E0/1e9**2)-E0/1e9)*1e9 # eV, proton KE
18    P = 5e3 # W, TFB peak power / electrode
19    Z = 100 # Ohm, TFB impedance / electrode
20
21    L = 935e-3 # m, TFB length
22    r = 70e-3 # m, TFB separation
23
24    E = T + E0 # Total Energy
25    gamma = E / E0 # Normalized energy (lorentz)
26    beta = np.sqrt(1-gamma**-2) # normalised velocity (lorentz)
27    cp = np.sqrt(E**2 - E0**2) # eV, particle momentum
28
29    # Electric Field
30    Vp = np.sqrt(P * Z * 2) # peak voltage
31    V = Vp * voltage
32    Efield = V / r # adjusted for gain
33
34    # Magnetic Field
35    I = np.sqrt((V**2/Z)/Z*2) # current
36    Hfield = (2*I) / (2*np.pi*r) # adjusted for gain
37    Bfield = Hfield * mu0

```

```

37
38 # Angle
39 theta_M = c/1e9*Bfield*L / (cp/10**9)
40 theta_E = Efield/1e9*L / (cp/10**9 * beta)
41 theta = theta_E + theta_M
42 return theta

```

Listing B.1: Python code to calculate angle kick produced by the TFB system (subsection 3.1.3).

```

1 import numpy as np
2 import scipy.signal as sig
3
4 frev = 470000
5
6 def generate_afg_chirp(
7     chirp_length_time = 0.001,
8     turn_freq = frev,
9     chirp_middle = frev*0.325,
10    chirp_dev = frev*0.025,
11    sampling_freq = 1e9):
12 """
13 Generates a frequency-modulated single chirp signal, centered on 'chirp_middle'
14 ' [Hz], with a deviation of 'chirp_dev' [Hz], and a length of '
15 'chirp_length_time' [s].
16 """
17 chirp_time_samples = np.arange(0, chirp_length_time, 1/sampling_freq)
18 chirp_signal_samples = sig.chirp(chirp_time_samples,           # time array
19                                 chirp_middle-chirp_dev,   # start frequency
20                                 chirp_length_time,       # end time
21                                 chirp_middle+chirp_dev) # end frequency
22
23 chirp_lasts_for_turns = chirp_length_time * turn_freq
24
25 return chirp_time_samples, chirp_signal_samples, chirp_lasts_for_turns

```

Listing B.2: Python code to generate a single chirp signal as produced by the Arbitrary Function Generator (Figure 3.5).

Appendix C

Data and Plots